Chapter x

Attosecond Physics: Attosecond Streaking Spectroscopy of Atoms and Solids

Uwe Thumm[1], Qing Liao[1], Elisabeth M. Bothschafter[2,3], Frederik Süßmann[2], Matthias F. Kling[2,3], and Reinhard Kienberger[2,4]

[1] *J.R. Macdonald Laboratory, Physics Department, Kansas-State University, Manhattan, KS66506, USA*

[2] *Max-Planck Institut für Quantenoptik, 85748 Garching, Germany*

[3] *Physik Department, Ludwig-Maximilians-Universität, 85748 Garching, Germany*

[4] *Physik Department, Technische Universität München, 85748 Garching, Germany*

1. Introduction

Irradiation of atoms and surfaces with ultrashort pulses of electromagnetic radiation leads to photoelectron emission if the incident light pulse has a short enough wavelength or has sufficient intensity (or both)[1,2]. For pulse intensities sufficiently low to prevent multiphoton absorption, photoemission occurs provided that the photon energy is larger than the photoelectron's binding energy prior to photoabsorption, $\hbar\omega > I_P$. Photoelectron emission from metal surfaces was first analyzed by Albert Einstein in terms of light quanta, which we now call photons, and is commonly known as the photoelectric effect[3]. Even though the photoelectric effect can be elegantly interpreted within the corpuscular description of light, it can be equally well described if the incident radiation is represented as a classical electromagnetic wave[4,5]. With the emergence of lasers able to generate very intense light, it was soon shown that at sufficiently high intensities (routinely provided by modern laser systems) the condition $\hbar\omega < I_P$ no longer precludes photoemission. Instead, the absorption of two or more photons can lead to photoemission, where a single photon would fail to provide the ionization energy I_p[6]. For more than a century,

photoelectron spectroscopy has supplied information about the structure of atoms, molecules, and solid matter[1,6,7]. In conjunction with quantum theory, it was, and continues to be, instrumental in revealing the microscopic, electronic, and morphological properties of matter.

Starting in the 1990s, laser technology[8,9] had advanced to provide intense pulses of light short enough to resolve the nuclear motion in molecules[11-16] in experiments using mutually delayed pulses. By varying the delay τ between the first (pump) pulse and second (probe) pulse, stroboscopic pictures of the nuclear motion could be obtained by recording a movie-like stroboscopic sequence of events. Typically, these molecular (or atomic) movies were assembled in a destructive way: The pump pulse creates an excited state which, over a range of pump-probe delays, is stroboscopically imaged by dissociative ionization of the molecule (or ionization of the highly excited atom) by the ultra-short probe pulse, which destroys the particular sample under study. Typical lengths for the pump and probe pulses in such experiments are of the order of several femtoseconds (1 fs=10^{-15} seconds), short enough to resolve the rotational and vibrational motion of molecules as well as the largely classical, slow motion of highly excited Rydberg electron wave packets in atoms.

1.1 The advent of attosecond physics

More recently, starting in the new millennium, advances in laser technology enabled attosecond pulses which opened the door to attosecond physics[10-12]. Attosecond physics includes, (but is not limited to) a variety of phenomena that occur in strong laser fields. It is thus not surprising that the first attosecond light pulses were created by the interaction of strong laser fields with gaseous, atomic targets[11,12]. One attosecond is staggeringly short, 1 as = 10^{-18} seconds, and one attosecond compares to one second in the way one second compares to the age of the universe. The timescale

is so short that light in vacuum, which moves at a speed of 299,792,458 m/s, travels only about 3 nanometers (1 nm = 10^{-9} m) during 1 attosecond. Attosecond physics is therefore intrinsically connected *not only* to an ultrashort timescale but also to very small length scales[10].

Modern laser technology currently provides table-top laser systems in state-of-the-art laboratories that generate short pulses in the near-infrared (NIR) spectral range with peak intensities reaching 10^{22} W/cm^2, corresponding to electric field strengths in the range of 10^{14} V/m[13]. Such sources have not yet reached few-cycle pulse durations and have limited repetition rates in the sub-Hz range. The repetition rates of laser sources capable of exceeding peak intensities in the 10^{14} W/cm^2 range, however, reach 10 kHz and higher[14]. Optical parametric chirped pulse amplifier (OPCPA) lasers[15] have extended intense short-pulse generation to the mid-infrared and permit repetition rates in the 100 kHz range[16]. Laser pulses with intensities up to 10^{15} W/cm^2, in turn, are used to generate ultrashort radiation in the extreme ultraviolet (XUV) and soft x-ray range with pulse lengths down to 70 as[17-19]. While such attosecond pulses enable unprecedented resolution in time, their spectral width is of the order of several electron volts (eV), and thus tends to compromise precise measurements in the energy domain.

Which particles move at the speeds corresponding to attosecond timescales? Nuclear motion in molecules happens on much longer timescales, well above the attosecond threshold. This is on the order of tens of femtoseconds, or slower (Fig. x.1). The study of the formation and breaking of chemical bonds with (longer-duration) femtosecond laser fields has given rise to the field of Femtochemistry[9].

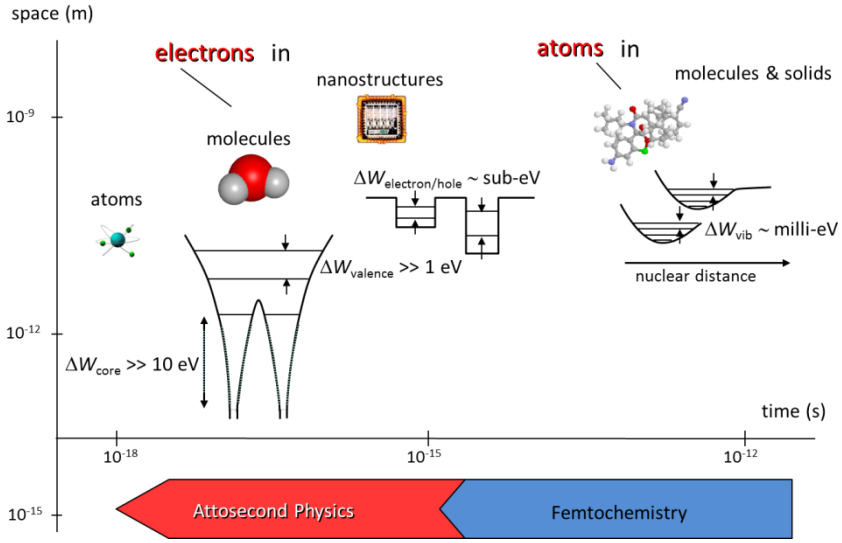

Fig. x.1: Time- and length scales for ultrafast processes. Adapted from [10].

For phenomena that happen at the attosecond timescale, we must turn to particles that are much lighter than the protons and neutrons of the nucleus– electrons. Electrons balance the positive charge of the atomic cores, form the glue for chemical bonds, and are responsible for electric conduction in solids (to name only a few examples). As an electron weighs about 1/1836 of a proton[20], their motion can occur *much* faster than the motion of nuclei, and they can also react much faster to an external electromagnetic force. As an example, one roundtrip of an electron in the first Bohr orbit in atomic hydrogen takes about 152 as[10]. More generally, the energy spacing of the involved electronic levels,$\Delta\varepsilon$,directly relates to the timescale of electron motion as shown in Fig. x.1[10].

1.2 Ultrashort laser pulses exert well-defined electromagnetic forces

Electrons (as charged particles) are susceptible to electric fields and can thus be driven by them. As electrons have very little mass, they can be driven at high frequencies, orders of magnitude above the current gigahertz–terahertz rates (10^9 – 10^{12} Hz) used in contemporary electronics.

Advances in laser technology have allowed tailoring the light wave's electric field (in the optical spectral region) with sub-femtosecond precision[21]. If this well-defined force is used to control electron motion, petahertz (1 pHz = 10^{15} Hz) lightwave electronics can be realized[22-24].

The electric field of a light pulse in the few-cycle domain may be described as

$$E(t) = E_0(t)\cos(\omega t + \phi_{CEP}) \qquad \text{(x.1)}$$

with envelope $E_0(t)$, carrier frequency ω, and the phase between the carrier wave and the envelope (carrier-envelope phase; CEP), ϕ_{CEP}. Examples of few-cycle pulses with different CEP values are shown in Fig. x.2. To utilize the CEP as a control parameter, the electric field waveform of a few-cycle laser pulse can either be stabilized[25] or precisely measured for each laser shot[26,27]. Light that is synthesized from ultra-broadband continua (spanning over more than one octave) permits *sculpting* of the electric field waveform with sub-cycle precision[21]. Such synthesized fields permit the control of electron dynamics on attosecond to femtosecond timescales.

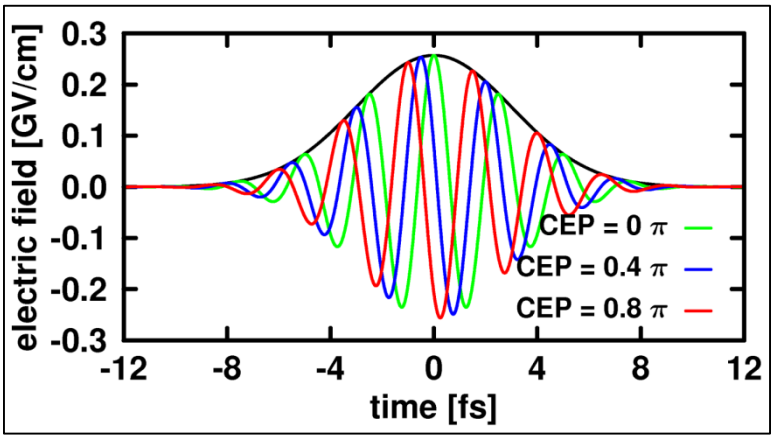

Fig. x.2: Carrier-envelope-phase (CEP) stable, few-cycle pulses at 800 nm. The electric fields for different CEP values are shown in color. The pulse envelope is indicated as a solid black line. Reproduced from [28] by permission of the PCCP Owner Societies.

The duration of such short pulses may be monitored with commercial dispersion-balanced autocorrelators or frequency-resolved optical gating devices (FROG)[29]. One of the most precise

ways to determine the sub-cycle evolution of the electric field of an intense laser pulse relies on the attosecond streaking technique[30,31], which will be introduced in Section 2.2.

1.3 Attosecond light pulses through high-harmonic generation

In most materials, electrons react so fast to external forces that their motion can be easily manipulated by a laser's electromagnetic field. Driven electron motion is at the heart of high-harmonic generation (HHG) and the creation of attosecond light pulses. HHG is most easily described by way of the three-step model [32]. Here, a strong laser field (strong enough to distort the Coulomb potential that binds an electron to an atom) results in tunnel ionization where an electron tunnels through a potential barrier (step 1). This electron is then accelerated in the field-dressed potential (step 2), and finally recollides with the core. This recollision results not only in the recombination of the electron with the atom, but also in the emission of high-energy photons (step 3). These photons have energies that are multiples of the photon energy in the driving laser pulses, see Fig. 3(a). The highest-energy photon that can be generated in this process is given by the classical cut-off formula

$$E_{max} = 3.17U_p + I_p \qquad \text{(x.2)}$$

where I_p is the ionization potential of the atom and $U_p$is the ponderomotive potential given as the average, classical kinetic energy of an electron in the laser's electric field

$$U_p = \frac{e^2 E_0^2}{4m_e\omega^2} \qquad \text{(x.3)}$$

with elementary charge e, electron mass $m_{e,}$ and the peak electric field E_0.

The first step requires high electromagnetic field strength and therefore occurs at (or near) the peaks of the external electric field. This leads to a good synchronization between the external field and the "birth" time of the electron (when the electron is emitted into the continuum). In the case of optical fields, this synchronization occurs on a sub-femtosecond timescale. The three-step, HHG process is repetitive and can occur near each peak of the driving laser field. Considering rare gas targets (or other targets with inversion symmetry) which are often used in HHG, this periodically driven electron rescattering process leads (for long driving pulses) to the emission of very distinct frequency combs with equidistant energy spacing $\Delta E = 2\hbar\omega$ [33]. Attosecond light pulses are generated by selecting and superimposing a sufficiently broad spectral range of (very) approximately constant spectral intensity in these combs, typically by sending the higher harmonic radiation through a thin metal foil. The generation of attosecond light pulses can be controlled by certain parameters of the driving laser field such as its polarization, frequency, waveform, envelope, and intensity, as well properties of the laser-target interaction (type of target, target density, laser caustic) [10,34-37]. A wealth of research has been devoted to the production of attosecond pulses and the use of HHG as a spectroscopic tool to explore attosecond phenomena in atoms and molecules (cf.,[38-42]). Using various techniques to limit HHG to below a single cycle of the driving pulse, the repetitive character can be interrupted, and isolated attosecond pulses can be generated[17,25,43-45]. These isolated pulses can be characterized by streaking measurements (see Section 2.2) and by making use of retrieval algorithms such as FROG-CRAB(Frequency-Resolved Optical Gating for Complete Reconstruction of Attosecond Bursts) [46,47] or PROOF (Phase

Retrieval by Omega Oscillation Filtering)[48]. The current record for the shortest, isolated attosecond pulses is 67 as [49], see Fig. x.3(b), covering a spectral range from 55 to 130 eV.

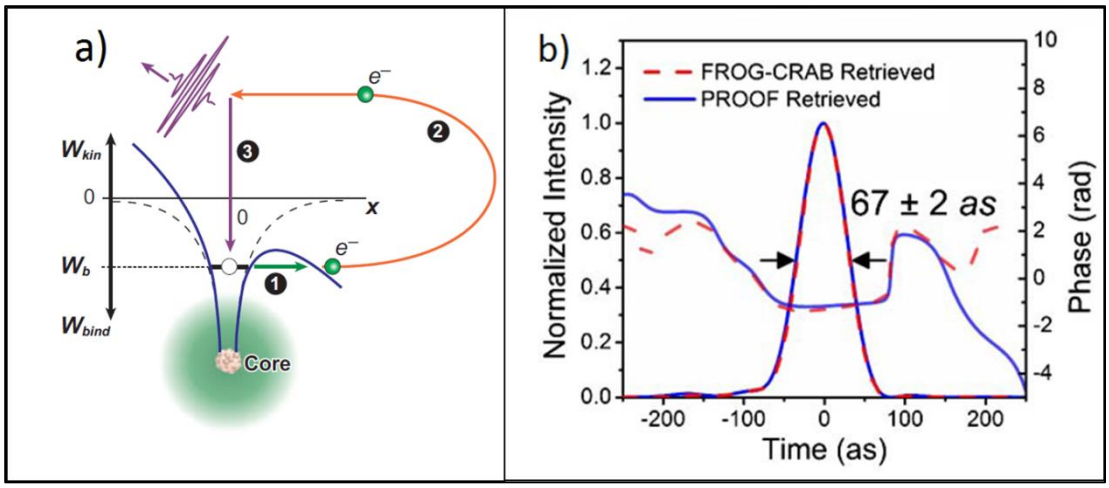

Fig. x.3: (a) High-harmonic generation process illustrated for an atom. Reprinted from[50] with copyright permission of Annual Reviews. (**b)** Retrieved pulse duration (with two retrieval algorithms indicated in the legend, for details see[49]) of an isolated attosecond pulse spanning a spectral range from 55 to 130 eV. Reprinted from[49] with copyright permission of OSA.

1.3 Time-resolving basic optoelectronic phenomena on an attosecond scale

Advances in attosecond metrology enabled the resolution in time of photo-ionization processes on their natural time scale (tens of attoseconds) for valence electron motion in atoms[11,51,52] and solids[53,54]. So far, this was mainly achieved through pump-probe experiments with intense, ultrashort NIR and XUV pulses of electromagnetic radiation. This ultrahigh time resolution allows for the unprecedented observation of an apparent time delay between the detection of multiple photoelectrons emitted by the same pulse of XUV photons but from different electronic levels of atoms and solids. Measured relative time delays for photoemission from different initial states are of the order of tens of attoseconds or less[54] and constitute accurate probes for the entirety of photoemission dynamics [53-57].

Time-resolved photoelectron emission experiments carried out by atomic, molecular, and optical (AMO) physics research groups have established "attosecond physics" as a promising research area[10,50,58-62]. Since the year 2007, attosecond physics has started to extend into solid-state physics, with the prospect of allowing the time-resolved observation of ultrafast electronic processes in metals[53,54,63], semiconductors, insulators[23,24,64,65], and nanostructures [66-68]. Time-resolved photoemission experiments at the intrinsic time scales of the correlated dynamics of two electrons [69-73]or the collective motion of many electrons [63,67,74] promise unprecedentedly sensitive experimental tests of electronic phenomena in solids and novel nanodevices[75,76]. The results of these tests will be relevant to lightwave electronics and the emerging field of nanophotonics [77].

In this chapter, we review the basic physics behind recent attosecond measurements of electronic dynamics in atoms, solid surfaces, and nanoparticles at a level accessible to a beginning physics graduate student. We will discuss time-resolved "dressed" (or "streaked") photoemission and photoemission delay times based on the comparison of calculated, time-resolved photoelectron spectra [4,53,63,78-88] with recent experiments[53-55]. Examined on an attosecond timescale, photoemission from atoms is sensitive to details in the modeling, such as the electronic structure of the target and the photoemission dynamics. The interplay of experimental and theoretical investigations in the field of attosecond physics therefore allows for extremely sensitive tests which enhance our understanding of electronic and photonic dynamics in matter. As compared to gaseous targets, for solid targets the understanding of streaked photoelectron spectra is further complicated by the substrate dielectric response [63] and electron-propagation effects[4,5,79,80] during the laser-assisted XUV excitation and emission processes. However, these "complications" could possibly offer a new approach for the time-resolved observation of collective (plasmon) excitations in large atoms, nanoparticles, and solids. As an added effect for attosecond time-resolved

photoemission from nanometer-sized particles, the influence of local electric (and magnetic) field enhancements near the particle's surface needs to be taken into account [77].

2. Time-resolved photoemission from atoms

2.1 Emission and characterization of photoelectron wave packets

Upon absorption of a photon, an atom may release a photoelectron. In this subsection we describe this process for model atoms exposed to short pulses of XUV radiation (Fig. x.4(a)). For simplicity, we only consider one spatial dimension. The generalization to three spatial dimensions, which more realistically accounts for the electronic structure and photoemission dynamics, is conceptually straightforward but technically more challenging.

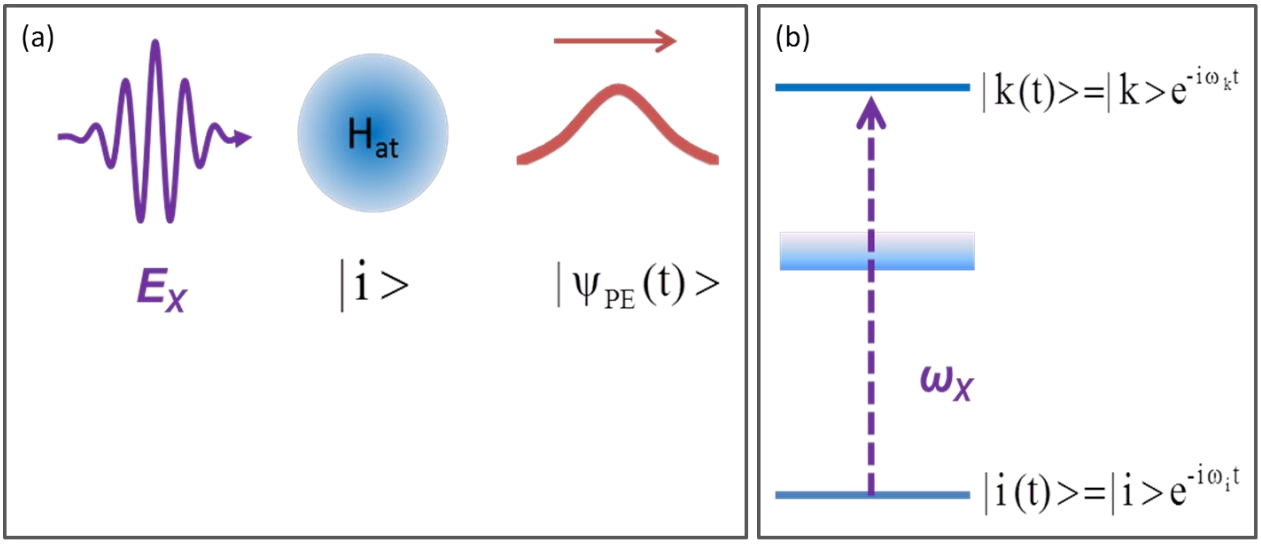

Fig. x.4:(a) Basic scenario for atomic photoionization by an ultrashort XUV pulse. The electric XUV field, E_X, acts on an atom as described by the Hamiltonian H_{at} and generates a photoelectron wave packet $|\Psi_{PE}(t)>$. **(b)** Schematic energy-level diagram. The absorption of one XUV photon results in electronic excitation from the bound atomic initial state $|i>$ with energy ω_i to a superposition of unbound continuum states $|k>$ of energy ω_k. At large distances between the photoelectron and the atom, this superposition forms $|\Psi_{PE}(t)>$.

We describe the model atom in terms of the atomic Hamilton operator H_{at} and assume that the atom is initially in a bound state, $|i>$. Absorption of one XUV photon with energy $\omega_X > I_P$ ionizes the atom by emitting an electron into a continuum state with energy ω_k and momentum k.

Here, and throughout this chapter, we use atomic units (a.u.), unless stated otherwise, for which $\hbar = 1$, elementary charge=1, electron mass=1, Bohr radius=1, $4\pi\varepsilon_0 = 1$. The initial bound and final continuum states of the active (photo)electron are given as solutions of the Schrödinger equation (SE),

$$H_{at}|i> = \omega_i|i> \; H_{at}\,|k> = \omega_k|k> \tag{x.4}$$

Disregarding all bound states with the exception of $|i>$, the general state of the atom after ionization is a superposition of the bound state and continuum states,

$$|\psi(t)> = g(t)|i(t)> \; + \int dk\; a_k\,(t)|\; k(t)> \tag{x.5}$$

Designating the electronic potential in the electric field, $E_X(t)$, of the XUV pulse as

$$V_X(t) = -\,zE_X(t) \propto z\int d\omega_X\,\tilde{\mathrm{E}}_X(\omega_X)e^{-i\omega_x t}, \tag{x.6}$$

the time-dependent coefficients in (x.5) are obtained by solving the time-dependent Schrödinger equation (TDSE)

$$i\tfrac{d}{dt}|\psi(t)> = [H_{at} + V_X(t)]|\psi(t)> \tag{x.7}$$

subject to the initial conditions

$$g(-\infty) = 1 \quad a_k(-\infty) = 0. \tag{x.8}$$

Consistent with our assumption that just one XUV photon is absorbed, we treat the XUV pulse as a weak perturbation and neglect couplings between continuum states by the XUV field. This means that we assume

$$< k|V_x|k' > \approx 0. \tag{x.9}$$

To first order in V_X, the expansion coefficients in (x.5) now follow as,

$$g(t) = 1 \quad a_k(t) = -i \int_{-\infty}^{t} dt' < k(t')|V_X|i(t') > \tag{x.10}$$

The second term in (x.5) describes the photoelectron wave packet. For sufficiently large times after the interaction of the XUV pulse with the atom, the wave packet has moved far enough away from the atom so as to no longer overlap with the initial-state wave function. By combining the second term in (x.5), (x.10), and (x.6), the photoelectron wave packet can be written as

$$|\psi_{\mathrm{PE}}(t) > \propto \int dk\, |k >< k|z|i > \tilde{\mathrm{E}}_X(\omega_{ki}) e^{-i\omega_k t} \tag{x.11}$$

that is, in terms of the spectral profile of the XUV pulse, $\tilde{E}_X$, and the dipole matrix element, $< k|z|i >$, with $\omega_{ki} = \omega_k - \omega_i$. Both factors are shown schematically in Fig. x.5. Owing to the limited range of the initial state in the configuration (and in momentum) representation, the dipole matrix element monotonously decreases at sufficiently large momenta, k. Assuming an XUV spectral pulse profile with a pronouced maximum at the momentum k_{max}^X, the photoelectron wave packet has its strongest spectral component at the momentum k_{max} close to and slightly red-shifted from k_{max}^X.

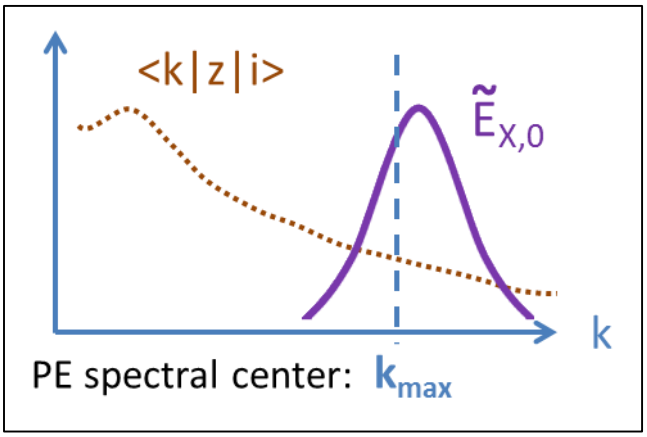

Fig. x.5: Sketch of the determinants of a photoelectron wave packet, generated by XUV photoemission, as a function of the momemtum k: dipole matrix element $< k|z|i >$ and envelope $\tilde{E}_{X,0}(k)$, of the spectral profile of the XUV pulse electric field $\tilde{E}_X(\omega_{ki})$. The dominant spectral contribution to the photoelectron wave packet has momentum k_{max}.

In position representation, the photoelectron wave function can written as

$$\psi_{\mathrm{PE}}(z,t) \propto \int dk\, |A(k)| \exp(\, i[arg < k|z|i > + kz - \omega_k t]) \qquad \text{(x.12)}$$

where the complex-valued expansion coefficients

$$A(k) = < k|z|i > \tilde{E}_X(\omega_{ki}) \qquad \text{(x.13)}$$

are separated into their magnitude, $|A(k)|$, and phase, $\arg(A) = arg\,(< k|z|i >)$. Taylor expansion of the phase of the dipole matrix element around the dominant momentum component,

$$arg < k|z|i >= arg < k_{max}|z|i > + \frac{d}{dk}\arg < k|z|i > |_{k_{\max}} (k - k_{\max}) + \ldots \,, \tag{x.14}$$

leads to the photoelectron probability density

$$|\psi_{\mathrm{PE}}(z,t)|^2 \propto \left| \int dk\, |A(k)| \exp(i\,[k(z - z_X) - \omega_k t]) \right|^2 \tag{x.15}$$

where we define

$$z_X = -\frac{d}{dk}\arg < k|z|i > |_{k_{\max}} . \tag{x.16}$$

The distance z_X can be thought of as the displacement of the photoelectron wave packet from a hypothetical reference wave packet with $z_X = 0$, while both wave packets propagate with the same group velocity, $v_g = d\omega_k / dk|_{k_{\max}}$ as illustrated in Fig. x.6.

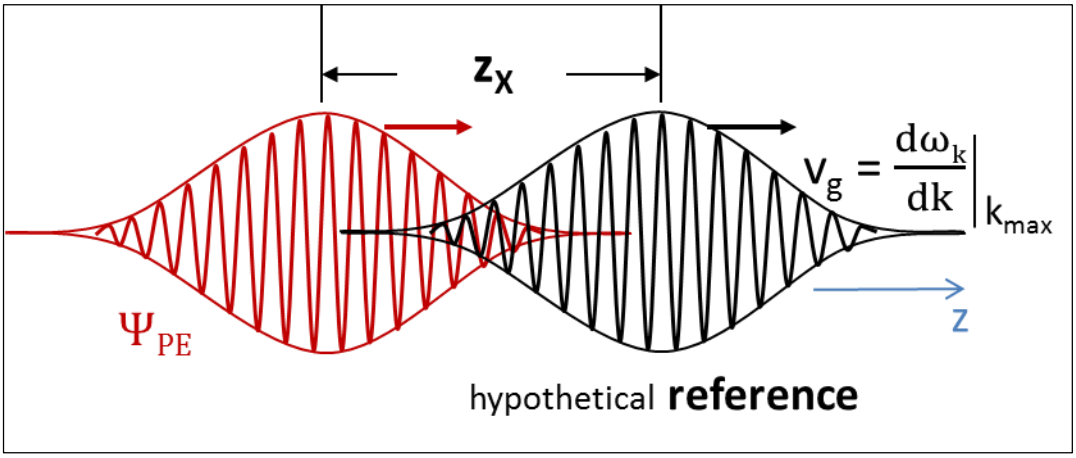

Fig. x.6: Displacement ,z_X, of the photoelectron wave packet $|\psi_{\mathrm{PE}}(t) >$,relative to a fictitious reference wave packet. Both wave packets move with group velocity $v_g$to a photoelectron detector. A photoemission time delay can be defined as $t_X = z_X/v_g$.

The time the photoelectron would need to catch up with the reference wave packet (if the reference wave packet could hypothetically remain stationary in space) defines the time delay,

$$t_X = z_X/v_{\mathrm{g}} \;\; = \; - \frac{d}{d\omega} \, arg \; < k|z|i > |_{k_{\mathrm{max}}}, \qquad \text{(x.17)}$$

where we assume free-electron dispersion, $\omega_k = k^2/2$, in the last part of the equation. Such a time delay was first introduced within the context of particle scattering. It can be related to the width (in energy) of scattering resonances and is often referred to as the'Wigner time delay'[89-91]. Mostly within particle scattering investigations, several definitions of time delays and so-called 'dwell times' were introduced in the past half century. (For a comprehensive review cf. Ref. [90]). For photoemission, a back-of-the-envelope approximation for the delay time, based on order-of-magnitude estimates for atomic and XUV parameters, shows that t_X is within the attosecond time domain. For $I_p =$ 10eV and ω_X =100 eV, $k_{max} \approx$ 2.6 and $v_g \approx$ 2.4. Taking the de Broglie wavelength, $2\pi/k_{max}$,as an upper limit for z_X now results in the upper limit of 1 a.u. = 24 attoseconds for t_X.

The delay time, t_X, can also be viewed as a delayed start time of a photoelectron relative to a non-delayed reference photoelectron by comparing the position expectation values of both wave packets (Fig. x.7) long after ionization[55,81,84,85],

$$< \mathrm{z} >= \lim_{n\to\infty} \; < \mathrm{z} >^{ref} - \mathrm{z}_X. \qquad \text{(x.18)}$$

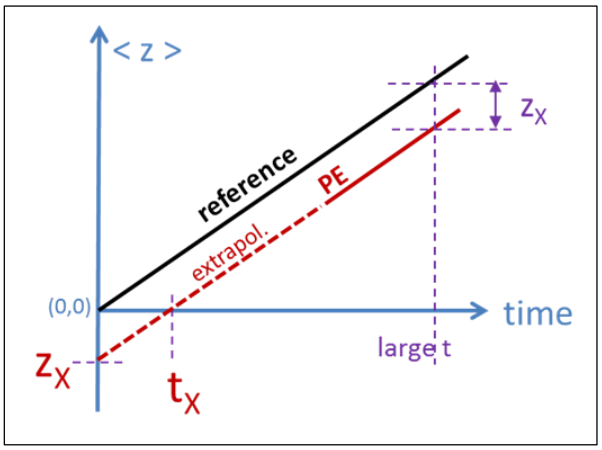

Fig. x.7: Interpretation of the photoemission time delay t_X, as delayed photoemission, starting at the position $z = 0$. Long after the photoemission, the photoelectron is assumed to move freely, is displaced by z_X from a reference wave packet, and its position expectation value $< z >=< \Psi_{PE}(t)|z|\Psi_{PE}(t) >$ is extrapolated to $z = 0$.

2.2 Influence of the IR streaking field on the photoemission process

Measurement of photoionization time delays requires a time reference. In theory, the time reference can be a reference wave packet, as discussed in Section 2.1. In practice, such a reference can be provided by simultaneously measuring photoemission from two energetically distinct initial states - of either the same target *or* two different targets - in the same streaked photoelectron spectrum. The energy mismatch of the two initial states needs to be large enough to be distinguishable in the photoelectron spectrum. For example, in order to measure time delays for photoionization of target atoms A, out of the bound state $|A: i >$, with an admixture of a gas of reference atoms B, that are ionized out of the state $|B: i >$, one would measure the *relative* time delay $\Delta t_{X,A-B} = t_{X,B} - t_{X,A}$.If the reference time delay $t_{X,B}$, is known, one can obtain $t_{X,A}$.

By measuring the time difference relative only to a single reference, the contributions of $t_{X,B}$ and $t_{X,A}$ to the absolute time delays which accumulate in exactly the same way cancel.

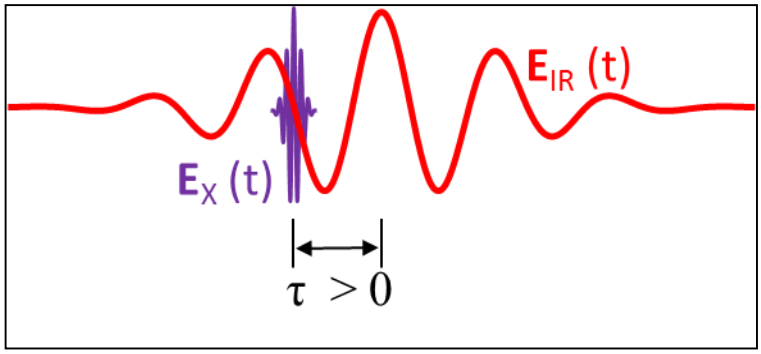

Fig. x.8: Streaked photoelectron spectra are obtained by recording XUV photoemission spectra for a range of delays ,τ, between the centers of the XUV pulse and IR laser pulse.

However, this lost information may be (to some extent) recovered by examining relative delays for different references and under different conditions, for example, with different XUV pulse parameters[82]. As the simple back-of-the-envelope example in Section 2.1 has shown, photoionization time delays are on the order of attoseconds and therefore many orders of magnitude too short to be resolved with state-of-the-art electronics. Instead, yet another reference is needed. Such a reference is provided by employing a second pulse of electromagnetic radiation, typically in the IR spectral range, with a fixed, but variable time delay τ relative to the center of the ionizing XUV pulse (Fig. x.8). The IR field modulates the photoelectron energy, and XUV photoelectron energies obtained as a function of τ are referred as "IR-streaked" photoemission spectra.

Recording XUV photoionization yields, assisted by delayed IR pulses, as a function of τ generates streaked photoelectron spectra that effectively convert photoemission time delays into photoelectron energy shifts. Thus, relative photoemission delays can be obtained by analyzing the temporal shift, (i.e., the phase shift τ between two streaking traces in the photoelectron spectrum, as shown schematically in Fig. x.9(a)). Assuming, for the time being, that the IR-pulse intensities

are small enough to prevent any distortion of the target's electronic structure, photoelectron streaking can be analyzed classically by solving Newton's equation

$$\frac{dp}{dt} = F = -E_{IR} \tag{x.19}$$

for the motion of a photoelectron that is released instantaneously at time τ by the XUV pulse into the IR electric field $E_{IR}(t)$ with momentum

$$p_0 = \sqrt{2(\omega_X - \omega_i)}. \tag{x.20}$$

For the initial electron momentum (x.20), integration of (x.19) yields the momentum long after the emitted electron has been subjected to the IR pulse,

$$p(\infty) = p_0 - A_{IR}(\tau), \tag{x.21}$$

in terms of the IR-pulse vector potential, $A_{IR}(\tau) = \int_\tau^\infty dt\, E_{IR}(t)$. The photoelectron momentum and energy registered by a photoelectron detector thus oscillate 180 degrees out of phase with the IR-laser electric field as a function of the delay between the XUV and IR pulses. Figure x.9(b) shows as an example a measurement of IR-streaked XUV photoemission from neon atoms with a measured relative photoemission delay of $\Delta t_{X,2p-2s} = (21 \pm 5)$ as [55].

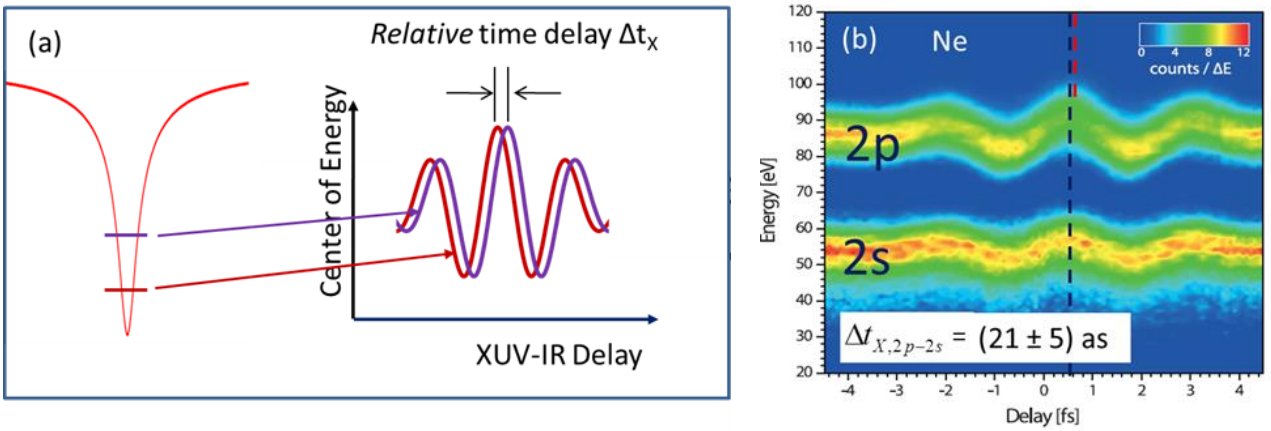

Fig. x.9:(a)
Illustration of the *relative* photoemission time delay ,Δt_X, for photoionization from two energetically separate atomic levels. The two initial states yield energetically separated streaking traces in the photoelectron streaking spectrum. Δt_X is obtained from the phase difference between the centers of energy of the two traces. **(b)** Measured photoemission streaking spectrum for XUV photoionization of Ne. The *relative* photoemission time delay for emission out of 2*s* and 2*p* levels is determined as $\Delta t_{X,2p-2s} = (21 \pm 5)$ as. Adapted from Ref.[55].

In practice, appropriate peak intensities of the IR streaking field are limited. A lower limit is given by the need to clearly resolve streaking oscillations, (i.e., by the energy resolution of the photoelectron detector). An upper limit is vaguely defined as the onset of distortions in the streaking spectra by the streaking IR field. The interpretation of streaked photoemission thus requires an understanding of the influence of the measurement itself (time to energy mapping in the IR field) on the measured observables: photoemission spectra and time delays. In the following subsections, we discuss this basic concern of quantum measurement. We will separately discuss effects that distortions of the *initial* and *final* quantum mechanical state of the active electron by the streaking electric field may have on photoemission spectra and time delays.

2.2.1 Initial-state perturbation

We examine the effect of a weak IR streaking field

$$E_{IR}(t) = E_{IR,0}\cos(\omega_{IR}t + \phi_{CEP}) \tag{x.22}$$

on streaked photoemission for model atoms with bound levels in which the excitation energy from state $|i>$ to an excited state $|e>$, is detuned by the energy $\Delta_{ei}(\omega_{IR})$ from the photon energy $\omega_{IR}$of the IR field (Fig. x.10). The influence of the IR field on the initial state of the target results in replacing the unperturbed initial state $|i>$in Fig. x.10 by the state

$$|\psi_i(t)> = g(t)|i(t)> + h(t)|e(t)>. \tag{x.23}$$

For the initial condition $g(-\infty) = 1,\ h(-\infty) = 0$, the TDSE for the active electron, including intra-atomic forces accounted for by the Hamiltonian H_{at}) and the force the photoelectron experiences in the IR laser field (in dipole approximation),

$$i\frac{d}{dt}|\psi_i(t)> = [H_{at} - zE_{IR}(t)]|\psi_i(t)> \tag{x.24}$$

yields, to first order in E_{IR},

$$g(t) = 1, h(t) = iE_{IR,0} < e|z|i > \frac{\sin(\Delta_{ei}t/2)}{\Delta_{ei}}\, e^{i(\Delta_{ei}t/2 - \phi_{CEP})} \tag{x.25}$$

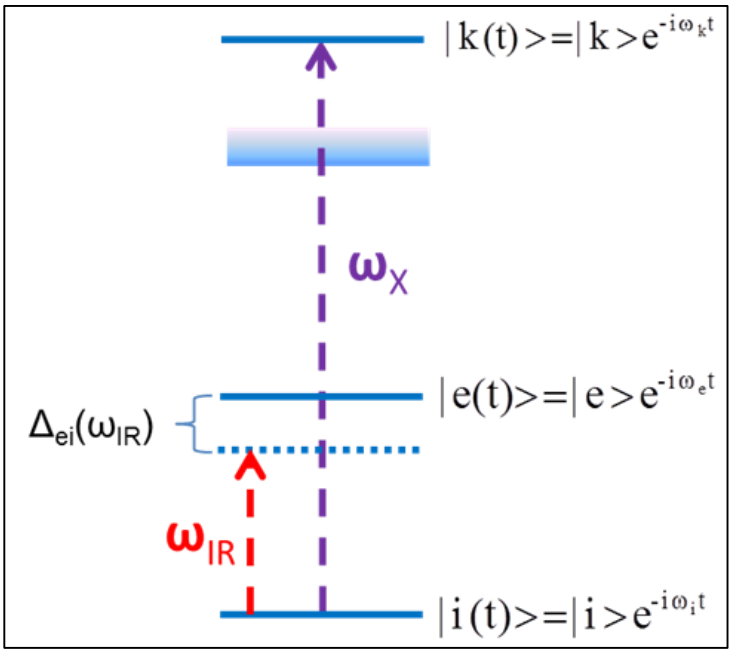

Fig. x.10: Schematic energy level diagram for XUV photoionization of an atom by absorption of a single XUV photon with energy ω_i in the presense of a streaking IR laser field of energy ω_{IR}. The streaking field perturbs the initial state |i > by coupling it to an excited state |e > that is detuned from resonance by $\Delta_{ei}(\omega_{IR})$.

Retracing the steps that lead to the photoelectron wave packet in Eq. (x.11), we see that the effect of the IR field on the photoelectron effectively amounts to replacing the dipole matrix element $< k|z|i >$ in (x.11) by

$$< k|z|i > \left[1 + iE_{IR,0}\frac{< k|z|e >< e|z|i >}{< k|z|i >}\frac{sin\Delta_{ei}}{\Delta_{ei}}e^{i(\Delta_{ei}/2-\omega_{ei})\tau - i\phi_{CEP}}\right] =< k|z|i > [1 + B] \quad \text{(x.26)}$$

where B is defined as the delay-dependent, complex-valued second term inside the second factor. Replacing the dipole matrix element in the XUV photoemission delay (x.17) with (x.26) and neglecting the influence of the IR field on both k_{max} and v_g yields the photoemission delay

$$t_{X,IR} \approx \; t_X - \frac{Re\,B}{v_g}\frac{d}{dk}\; arg\left\{< k|z|e > \; - \; < k|z|i >\right\}|_{k_{max}} \qquad \text{(x.27)}$$

in which the IR electric field appears as an additive, linear perturbation (second term) to the unperturbed delay t_X. The IR-field-dependent term is largest at resonance where $\Delta_{ei} = 0$. It oscillates with the XUV-IR delay so that within this perturbative analysis, (i.e., for sufficiently small $E_{IR,0}$) the influence of the streaking field on the photoemission time delay tends to cancel (on average) over one IR period. The oscillation occurring with the delay is a result of measuring t_X and distorts the sinusoidal behavior of the streaking traces in the photoelectron spectra as predicted - without taking the streaking field into account - by Eq. (x.21). As an example of the signature of the initial-state perturbation on streaked photoemission spectra, Fig. x.11 shows numerical results obtained for one-dimensional, model hydrogen atoms in which the electron and nucleus interact via the soft-core Coulomb potential

$$V(x) = \frac{-1}{\sqrt{x^2+a^2}}. \qquad \text{(x.28)}$$

The parameter a is adjusted to the ionization energy of hydrogen atoms (13.6 eV). The calculation was performed with the following parameters: for the XUV pulses, a central energy of 25 eV and a pulse length of 200 as were used; for the streaking IR pulses, a wavelength of 800 nm at a peak intensity of 2×10^{12} W/cm^2 and a pulse length of 5 fs[82] were employed. For photoionization from the relatively strongly bound ground state, the streaking field's effect on both the photoelectron spectrum and the streaking trace's center of energy is very small [Fig. x.11(a-c)]. In contrast, for

photoionization from the model atom's first excited state, the streaking field severely distorts the central energy and the sinusoidal shape of the unperturbed streaking trace [Fig x.11(d-f)].

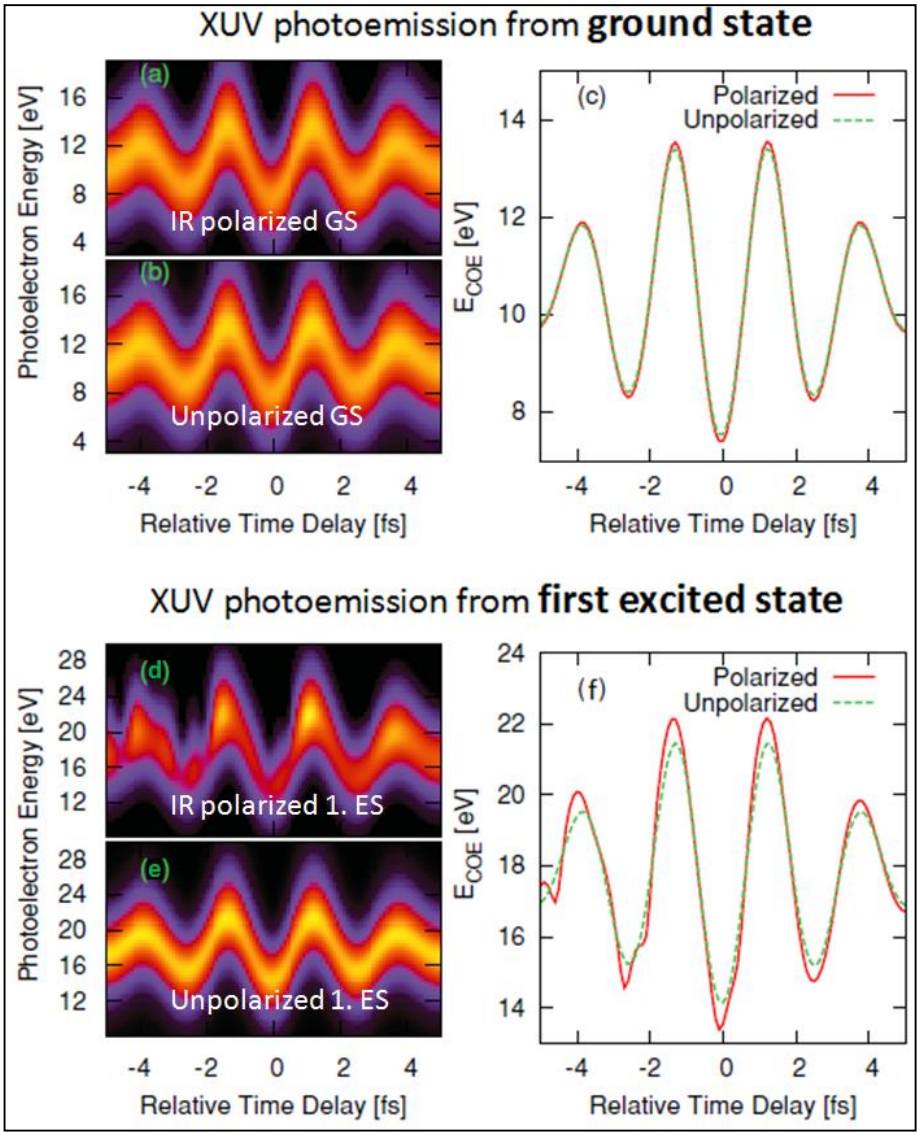

Fig. x.11: The effect of initial-state perturbation (here referred to as "polarization") by the IR streaking field on XUV photoemission from the ground state of a 1-dimensional model hydrogen atom for $\hbar\omega_X = 25$ eV XUV pulses with a pulse length of 300 as. **(a)** Spectrogram including initial state polarization. **(b)** Spectrogram without initial state polarization. **(c)** Corresponding central energies $E_{COE}(\tau)$ obtained as first moments in energy from the streaking traces. **(d,e,f)**: same as **(a,b,c)** for XUV photoionization from the first excited state of the model hydrogen atom. Adapted from Ref. [82].

2.2.2 Final-state interactions

In deriving the streaking momentum of the emitted photoelectron in Eq. (x.21), we assumed that the active electron is instantaneously released by the absorption of one XUV photon, and that the photoelectron continues to move classically *solely* under the influence of the electric field it experiences in the IR streaking pulse. All other forces, such as the interaction of the photoelectron with the residual ion, are excluded in this approach. The implementation of this idea – the sudden release of a photoelectron and subsequent disregard of all but the IR-laser field – within a quantum mechanical model is straightforward and referred to as "strong-field approximation (SFA)" (Fig.x.12)[4,5,82,92]. The SFA takes advantage of the fact that the TDSE for the motion of an electron that is exposed solely to an oscillating electromagnetic field can be solved analytically. The corresponding closed-form solutions are the so-called Volkov states[6,93]

$$|k(t)>^{Volkov}= |k + A_{IR}(t)> e^{i\Phi(t)}. \qquad \text{(x.29)}$$

The Volkov phase

$$\Phi(t) =-\frac{1}{2}\int^{t} dt' \ [k^2 + 2kA_{IR}(t') + A_{IR}(t')^2] \qquad \text{(x.30)}$$

includes three terms with a distinct physical meaning. The first term simply corresponds to the kinetic energy, $k^2/2$of a free electron with momentum k. The second and third terms depend on the streaking field. The second term represents the energy shift that the active electron experiences due to the streaking field and explains the energy oscillations in photoelectron streaking spectra with $-kA_{IR}(\tau)$. This is consistent with the classical derivation of the final photoelectron

momentum in Eq. (x.21). The third (so-called "ponderomotive") term is the energy associated with the photoelectron's quiver motion in the streaking field and can be neglected for typical streaking field intensities.

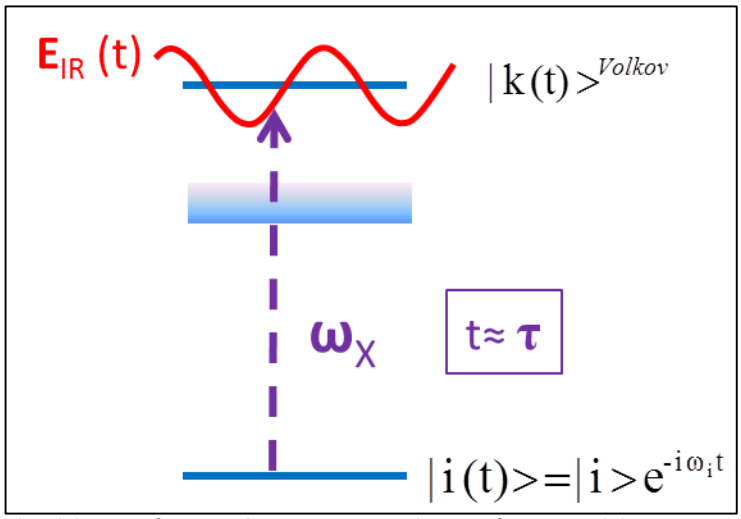

Fig. x.12: Schematic energy level diagram for XUV photoemission at the specific XUV-IR delay τ. In strong-field approximation the final photoelectron state $|k(t)>^{Volkov}$ is modeled as an eigenstate of the photoelectron in the electric field, $E_{IR}(t)$, of the IR laser field.

The SFA allows photoemission streaking spectra to be easily modeled in quantum mechanical calculations by replacing the free final state of the photoelectron in Eq. (x.9), $|k(t)>$, with the Volkov state (x.29)[4,5,82,92]. Since the oscillatory behavior of the streaking traces is explained by the Volkov phase (x.30) alone, the question arises to what extent photoemission streaking spectra and time delays are affected by replacing the free-electron momentum eigenstate $|k>$, in the phase $arg<k|z|i>$ of the dipole matrix element in Eqs. (x.12) and (x.13) with the state $|k + A_{IR}(\tau)>$ corresponding to the electron's kinematic momentum in the field. We seek an answer to this question by expanding the phase of the IR-field-dressed dipole matrix element in both, $A_{IR,0}$ and the momentum difference $k - k_{max}$.Since k-independent terms do not change the photoelectron probability density (x.15), we do not keep these terms and obtain

$$arg < k + A_{IR}(\tau)|z|i > = -\{z_X + \Delta z_{IR}(\tau)\}\, k + O\left(A_{IR,0}^2; [k - k_{max}]^2\right), \qquad \text{(x.31)}$$

with the definition

$$\Delta z_{IR}(\tau) = \frac{d^2}{dk^2} arg < k|z|i > |_{k_{max}} A_{IR}(\tau). \qquad \text{(x.32)}$$

The presence of the streaking field thus adds the displacement Δz_{IR} to the IR-field-free displacement z_{IR} in Eq. (x.16) and Fig. x.6. Consequently, the IR field changes the field-free photoemission time delay t_X in Eq. (x.17) to

$$t_{X,IR}(\tau) = \frac{z_X + \Delta z_{IR}(\tau)}{v_g + A_{IR}(\tau)} = t_X + \Delta t_{IR}(\tau) + O(A_{IR,0}^2), \qquad \text{(x.33)}$$

with the first-order correction

$$\Delta t_{IR}(\tau) = \frac{\Delta z_X}{v_g} - t_X \frac{A_{IR}(\tau)}{v_g}. \qquad \text{(x.34)}$$

The first term in the IR-field-induced temporal shift, Δt_{IR}, corresponds to the extra time the photoelectron needs to cover the displacement Δz_{IR} at the group velocity v_g. The second term accounts for the IR-laser-induced change of the group velocity in the denominator of Eq. (x.33). Δt_{IR} oscillates with the XUV-IR delay τ, and vanishes in the average over one IR period (for

sufficiently long IR pulses). Averaged over the IR-laser period, the change of the phase in (x.31), $\Delta z_{IR}(\tau)k$, due to a weak streaking field therefore does not affect relative photoemission time delays. IR-laser-induced changes in (x.31) can, however, modify the shape of the photoelectron dispersion wave packet in streaking traces; this is similar to the effect of initial-state distortions discussed above (cf., Fig. x.11).

2.2.3 Coulomb-laser interactions

For theoretical studies of streaked photoelectron spectra and photoemission time delays, the SFA is a convenient scheme thanks to a particularly simple representation of the photoelectron's final state. The availability of a closed-form expression for the final-state wave function of the photoelectron facilitates photoemission calculations significantly. In addition, quantum-mechanical photoemission streaking calculations with Volkov final states yield streaking traces that follow, without distortion, the laser vector potential. This is in agreement with the simple classical result for the final photoelectron momentum, Eq. (x.21). In order to examine to what extent effects that are not accounted for in the SFA influence streaked photoemission spectra, we proceed by assuming the results of the SFA calculations as a reference[82].

An important shortcoming of the SFA is its complete neglect of the interaction between the emitted electron and the residual, positively charged ion. In order to include this interaction (i.e., both the influence of the streaking laser's electric field and the residual ion's Coulomb field) on the motion of the photoelectron, we seek an approximation for the full Coulomb-Volkov final-state wave function that goes beyond the SFA. For clarity and simplicity, we continue to illustrate our discussion with numerical results of a one-dimensional simulation of the photoionization process. For a single-active-electron description in full dimensionality see Ref.[94].

From the SFA analysis we learned that the streaking of photoelectron energies in the IR laser electric field is approximately represented by the phase of the final-state wave function. Taking the SFA as a guide, we now write the final-state wave function as

$$\psi_k^{EA}(x,t) \sim e^{-ik^2\, t/2 - iS^{EA}(x,t)} \tag{x.35}$$

and split the action function, S^{EA}, into two parts – the known action in the SFA, S^{SFA}, and a to-be-determined action, S^{CL},

$$S^{EA} = S^{SFA} + S^{CL} \tag{x.36}$$

In order to determine S^{CL}, we apply the semiclassical eikonal approximation (EA)[6,82,94]. In EA, the quantum mechanical wave function is written in the form of Eq. (x.35), and the action, S^{EA}, is determined classically by calculating the phase accumulation along classical electron trajectories $x_{free}(x,t') = x + k\,(t-t')$that start at position x at time t. For the motion of photoelectrons subjected to the potential of the residual ion, $V_{Ion}(x)$, *and* the laser electric field, the accumulated "Coulomb-laser (CL)" phase (x.36) is given by

$$S^{CL}(x,t) = \int_t^{\infty} dt' \, \frac{\delta V_{Ion}\left[x_{free}(x,t')\right]}{\delta x_{free}} \Delta x(t') + O\left(A_{IR,0}^2\right). \tag{x.37}$$

In classical mechanics (expressed in terms of action and angle variables), the negative time derivative of an action results in an energy [95]. Here, the time derivative of S^{EA} with (x.37) results in the expression

$$\delta E^{EA}(x,\tau) = -\frac{\delta S^{EA}(x,t)}{\delta t}\Big|_{\tau} = -\left[k + \frac{|V_{Ion}(x)|}{k}\right] A_{IR}(\tau) + \int_{-\tau}^{\infty} dt\ \frac{\delta V_{Ion}[x'(t)]}{\delta x'} A_{IR}(t) \quad \text{(x.38)}$$

for the energy shift in the IR streaking field. The first term in this formula is the familiar streaking shift in the SFA,

$$\delta E^{SFA}(\tau) = -\frac{\delta S^{SFA}(t)}{\delta t}\Big|_{\tau} = -kA_{IR}(\tau)\,. \quad \text{(x.39)}$$

The second and third terms include the combined interaction of the photoelectron with the laser and Coulomb fields. In our numerical applications for typical streaking parameters[82], we find that the third term can be neglected in comparison with the second term.

In order to reveal changes –relative to the SFA predictions – in the streaking amplitude and photoemission delay due to the simultaneous interaction of the emitted photoelectron with the Coulomb and IR-laser fields, we fit local amplitude and delay functions, $K(x)$ and $\Delta t_X(x)$, to the streaking shift (x.38),

$$\delta E^{EA}(x,\tau) = -K(x)A_{IR}[\tau - \Delta t_X(x)]. \quad \text{(x.40)}$$

Numerical tests for streaked photoemission from one-dimensional model hydrogen atoms with the soft-core Coulomb potential (x.28)[82], show dominant contributions to the local streaking shift at $x = 0$ where the initial-state wave function is localized. Numerical results for the same target atom also show very close agreement between the EA and full TDSE solutions, while TDSE calculations deviate noticeably from results obtained in SFA.

Figures x.13(a) and (b) show streaked photoemission spectra for an IR field with a peak intensity of $2\times10^{12}\,\mathrm{W/cm^2}$. Here, the XUV pulses have a pulse length of 300 as and central photon energies of 90 eV [Fig. x.13(a)] and 25 eV [Fig. x.13(b)]. Figure x.13(c) shows the corresponding centers of energy relative to the SFA shift (x.39). The centers of energy are evaluated as first moments of the streaking traces in Fig. x.13(a) and Fig. x.13(b), respectively. The two curves are shifted by 50 as. The deviation from the SFA results for $\hbar\omega_X = 90$ eV are smaller than for 25 eV, as one would expect in view of faster photoelectrons being affected less by their interaction with the residual ion.

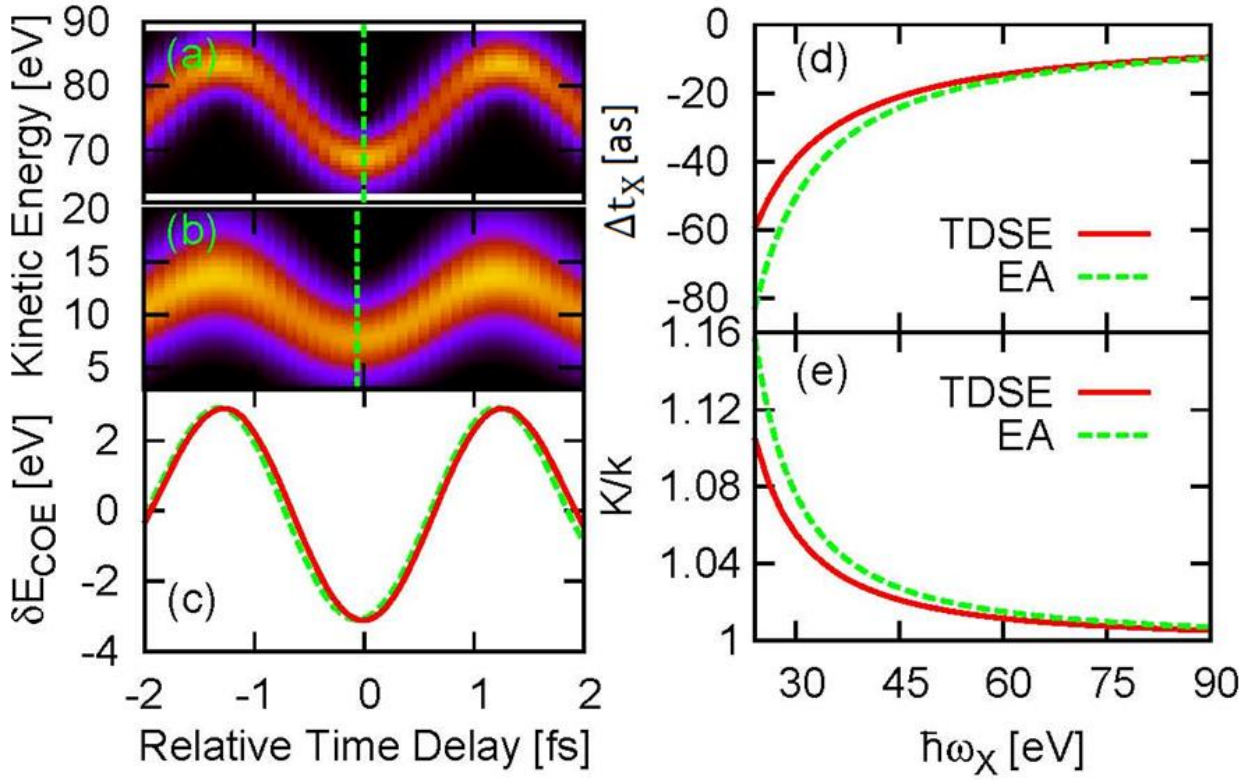

Fig. x.13: Streaked photoemission from model hydrogen atoms. Results obtained by numerically solving the time-dependent Schrödinger equation (TDSE) for XUV pulses with **(a)** $\hbar\omega_X = 90$ eV and **(b)** 25 eV. **(c)** Corresponding center-of-energy shifts $\delta E_{COE}(\tau)$ for $\hbar\omega_X = 90$ eV (solid line) and 25 eV (dashed line). To facilitate the identification of the temporal shifts Δt_X $\delta E_{COE}(\tau, \hbar\omega_X = 90\ eV)$ is normalized to the $\hbar\omega_X$ =25 eV result. **(d)**$\Delta t_X(x = 0)$and **(e)** oscillation amplitude $K(x = 0)$ in Eq. (x.40) relative to the strong-field approximation (SFA) for TDSE (full line) and eikonal-approximation (EA, dashed line) calculations. Adapted from Ref.[82].

In Figs. x.13(d) and (e) we compare EA results with TDSE results for XUV photon energies between 25 and 90 eV. Figure x.13(d) compares the change in photoemission time delay relative to the SFA photoemission delay, obtained by fitting Eq. (x.40) and evaluated at $x = 0$, with the prediction of full TDSE calculations. Figure x.13(e) shows the amplitude $K(x = 0)$ in EA relative to the SFA streaking amplitude k obtained by fitting Eq. (x.40) to Eq. (x.38). The EA and TDSE results are in good agreement and converge, as expected, to the SFA results for higher photoelectron energies.

3. Streaked photoemission from solids

3.1 Principle and setup for fs to sub-fs time-resolved experiments on surfaces

Near-IR (NIR)-dressed, attosecond XUV-photoemission spectroscopy, as described in the previous sections, can be used to investigate fs to sub-fs dynamics in solids. In order to apply this spectroscopic method to the study of surface-electron dynamics, special experimental conditions are necessary which are introduced here first. We then review some benchmark experimental results achieved with this method[54,96,97], which shall give a taste of the exciting insights into surface dynamics and spectroscopy that can be expected when investigating the ultrafast interaction of solid-state systems with attosecond light pulses.

The most direct access to electron dynamics in regions near a surface is granted by photoemission, since the typical escape depth (taken as the electron mean-free path (MFP), λ) of photoelectrons excited by XUV photons is in the range of 5-10 Å, which corresponds to only 2-3 lattice constants[98]. Conceptually, the simplest way to resolve attosecond dynamics by photoemission would be to perform pump-probe measurements using attosecond XUV pulses for both, triggering and probing excitations in the substrate as it is done in the femtosecond domain with UV 2-photon-photoemission (cf.,[99]). However, this approach is so far stymied by the low intensities available from contemporary high-harmonic light sources. Nevertheless, a high time resolution can be achieved by using the attosecond streaking technique, where single-photon photoionization is initiated by an XUV pulse in the presence of a strong NIR laser field. If the duration of the XUV-induced photoelectron wave packet becomes shorter than half the period of the dressing field (~1.3 fs for NIR pulses) the wave packet's energy is modified according to the vector potential of the dressing field at the instant of emission. This technique was introduced in Section 2.2 as a tool for characterizing light pulses and electronic dynamics with sub-fs time resolution.

The NIR-induced energy shift in streaked electron spectra is highly dependent on the time when the electrons enter the laser-dressed continuum. Therefore, relative photoemission time delays, Δt_X, between the release of photoelectrons from different electronic states in a solid can be resolved by varying the relative delay, τ, between the NIR and the XUV pulse, since any time delay in emission will be mapped in streaked photoemission spectra as a relative shift between the streaking traces along the NIR-XUV delay axis (cf., Section 2.2).

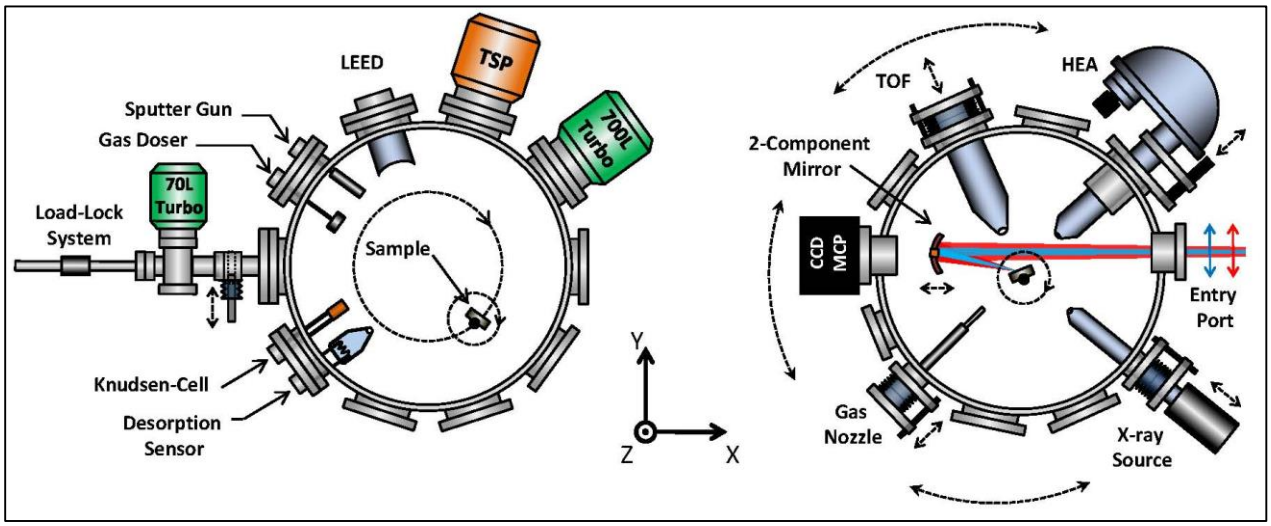

Fig. x.14: Apparatus for attosecond photoemission experiments in UHV. The sample is transferred from ambient into the preparation chamber (left), where an atomically clean surface can be prepared under UHV conditions. The UHV conditions are achieved and maintained by combining standard turbomolecular pumps (Turbo) with liquid nitrogen-cooled titanium sublimation pumps (TSP) and high temperature bake-out after each venting procedure. The quality of the surface preparation can monitored with low-energy-electron-diffraction (LEED). Atomic mono- and multilayers of various materials can be evaporated onto the sample with a Knudsen-cell and calibrated with a desorption sensor. The attosecond photoemission experiments are performed in a second UHV chamber (right), which is connected to the NIR-XUV beamline and incorporates two electron energy analyzers, a simple time-of-flight (TOF) electron spectrometer and a hemispherical analyzer (HEA) for resolving also the lateral momentum. The various degrees of freedom for the positioning of individual components are indicated by dashed arrows (from [96] with copyright permission of Springer). A charge-coupled device (CCD) combined with a XUV-sensitive multi-channel plate detector (MCP) allow for detection and optimization of the XUV beam profile before sending both the XUV and the NIR beam on the 2-component mirror.

The typical experimental setup necessary for attosecond streaking measurements on solids as presented in Ref.[96] is summarized in Fig x.14: High-harmonic (HH) radiation is generated by exposing neon atoms to intense, waveform-controlled, few-cycle NIR laser pulses (violet beam). A thin metal filter spatially separates the low-divergence XUV radiation (blue beam) from the

residual NIR light. The two collinear beams are reflected by a two-component mirror. The outer portion of this mirror is fixed and focuses the NIR pulses onto the sample while the inner part serves as a band-pass reflector in order to filter isolated sub-fs XUV pulses from the HH cutoff continuum. Moving the inner mirror back and forth changes the length of the pathway for the XUV pulses and therefore introduces a delay between the XUV and NIR pulses. This is made possible by a piezo-electric translation stage onto which the inner mirror is mounted. Both pulses are spatially and temporally overlapped on the sample surface positioned in the focus of the double mirror assembly[100]. The kinetic energies of the XUV-induced photoelectrons emitted along the surface normal are analyzed by a time-of-flight spectrometer (TOF) as a function of the relative delay between the NIR and XUV pulses.

Due to the high surface sensitivity of XUV photoemission, the experiments must be performed under excellent ultrahigh vacuum (UHV) conditions (base pressure $<10^{-10}$ mbar) to avoid the disrupting influence of adsorbed atomic impurities on the surface [101]. The end-station used for the experiments presented in the next section is divided into two segments. The first chamber accommodates several surface-science diagnostic tools such as a sputter gun, evaporators, a gas-dosing system, and a low-energy electron diffraction (LEED) system, which are necessary for preparing and characterizing atomically clean, single-crystal surfaces and well-defined adsorbate layers[98]. Sample transfer from the ambient into the UHV system is enabled by a load-lock system. The sample is mounted on a motorized, 360° rotatable *XYZ*-manipulator. Full temperature control of the sample (in the range of ~10-2,500 K) is provided by an integrated flow-cryostat (operated with liquid helium) and the combination of heating filaments with a variable sample potential up to ~1 kV. The second chamber is connected to the NIR-XUV beamline and is dedicated to attosecond streaking experiments. It houses different electron analyzers (e.g., TOF or

hemispherical energy analyzer, HEA) and the double-mirror assembly. A cross-sectional view of the UHV system is schematically depicted in Fig. x.14

3.2 Photoemission delay measured for tungsten surfaces

In the case of multiple, distinct emission lines in the photoelectron spectrum, the attosecond streaking technique can be used to compare the characteristics of photoelectrons originating from the different states. For example, the photoelectron spectrum of a (110)-oriented tungsten surface obtained with attosecond XUV pulses (Fig. x.15) shows two distinct peaks originating from 5d/6sp valence/conduction band (VB, CB) electrons and 4*f* /5p core levels. By employing the attosecond streaking technique, the relative timing of the photoelectron emission, the instant when they leave the surface, can be determined.

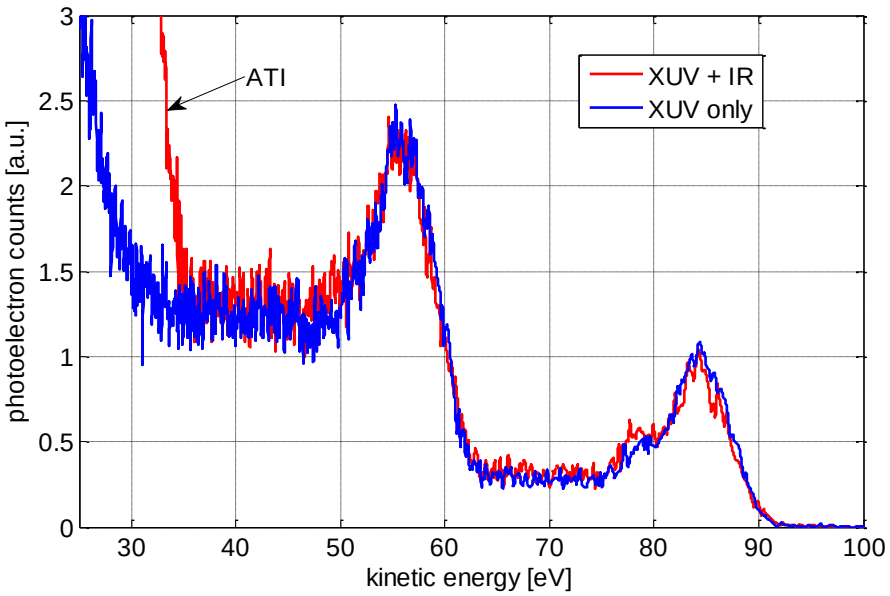

Fig. x.15: Raw photoelectron spectra of tungsten (110) measured with (red curve) and without (blue curve) the presence of the probe NIR streaking field using 91 eV, XUV photons. The spectra show two distinct peaks originating from *5d/6sp* valence and *4f/5p* core levels at ~83 and ~56 eV, respectively. In the presence of the NIR probe field, there is an intense photoelectron signal below 35 eV induced by above threshold ionization (ATI). Each spectrum was obtained by integration over 60,000 laser pulses.

As is illustrated in Figure x.16, photoelectrons leaving the surface at different instants are subjected to different phases of the streaking field. It is possible to extract an effective emergence time for

the electrons using the waveform-controlled streaking field[31]. Here we ignore the streaking field inside the solid which, due to the metal's optical properties, is weak[102]. As a result, the effective delay in photoemission can be reconstructed from the spectrograms.

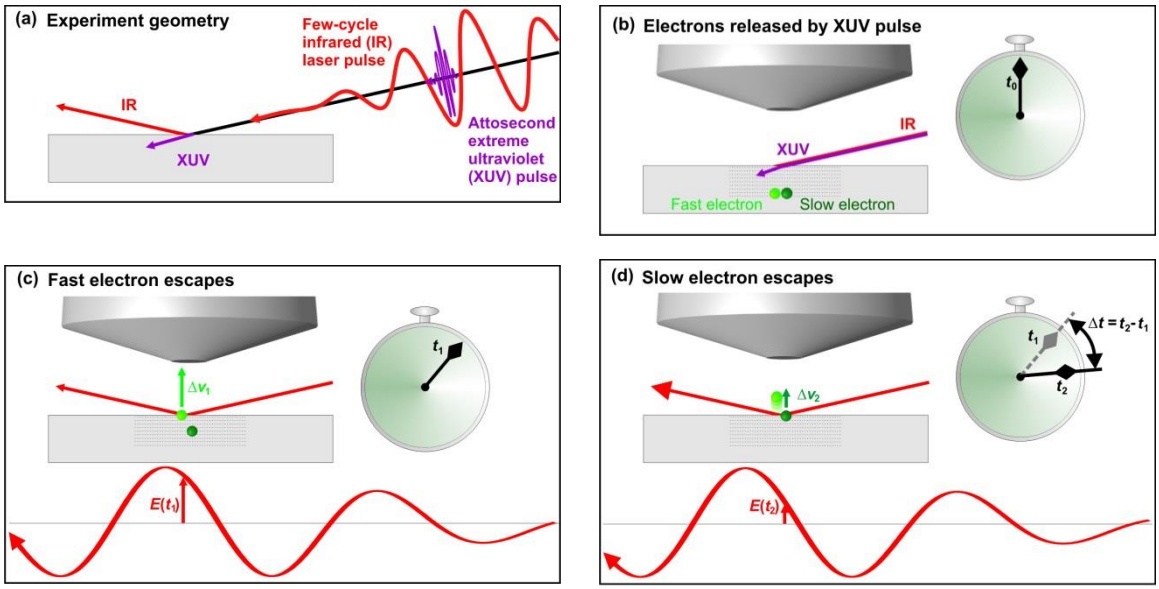

Fig. x.16: Attosecond spectroscopy on solids: Electrons arriving at the surface at different instants are subjected to different phases of the streaking field outside the metal. In panel **(a)** an isolated attosecond XUV pulse and a delayed few-cycle, waveform-controlled streaking field are incident on a solid surface. In panel **(b)**, at time t_0, the XUV pulse is absorbed in the solid and two types of photoelectrons are born, for simplicity one photoelectron is called "slow," the other "fast". In panel **(c)**, at time t_1, the fast electron has propagated to the surface and is now subjected to the strong streaking field, which modulates its outgoing kinetic energy which is dependent on the instant of release. In panel **(d)** at time t_2, the slow electron has reached the surface and feels the strong streaking field on the vacuum side; since it has emerged at a different time, the modulation of its kinetic energy will vary depending on the precise delay in emission. By evaluation of the full streaking spectrograms, collected as a function of relative delay between the attosecond XUV pulse and the streaking field, the delay in photoemission can be determined. Compared to streaking experiments at isolated particles, detailed models of electron localization, and electron and photon transport and interactions in the surface are necessary for the evaluation of such spectrograms (from[97] with permission from Wiley).

A tungsten (110) surface was the sample used in the first proof-of-principle experiment[53]. From clean W(110), two nearly parallel spectrograms are observed that originate from different electronic bands, the *5d* valence and *6sp* conduction band, and the *4f/5p* core level band, which are emitted with different kinetic energies (Figure x.17(a)). The large bandwidth of the excitation pulse does not allow separation of the 4*f*/5*p*, and the 5*d*/6*sp* intensities, respectively. However, due

to their comparatively small ionization cross sections and densities of states, the *5p* and *6sp* contributions are minor, and the spectra are dominated by *5d* valence and *4f* core emission lines. Both spectrograms show the change in electron energy corresponding to the evolution of the electric field of the NIR streaking pulse. Figure x.17(b) shows a center-of-mass (COM) analysis of the spectrograms. For this analysis, the time-dependent COM of both emission lines were calculated in a global fit of the function:

$$COM\,(\tau) = a\, e^{-4\ln(2)\frac{(\tau - t_0 - \Delta t_X)^2}{FWHM^2}} \sin(\omega\tau + \phi_{CEP} - \omega\Delta t_X) + offset \qquad \text{(x.41)}$$

where a , and $offset$ denote the respective streaking amplitudes and the time-independent positions of the emission lines. t_0 and *FWHM* denote center and full width at half maximum of the Gaussian-shaped envelope of the streaking field, and ϕ_{CEP}gives its carrier envelope offset phase. The relative photoemission delay Δt_X accounts for a temporal shift between the spectrograms of both emission lines. The fit results are shown as solid lines in Figure x.17(b), and a temporal shift in the streaking of Δt_X =85 ± 45 as is extracted. This result is in good agreement with the initial study, where the valence electrons were found to be emitted approximately 100 attoseconds earlier than their tightly bound core-state counterparts[53].

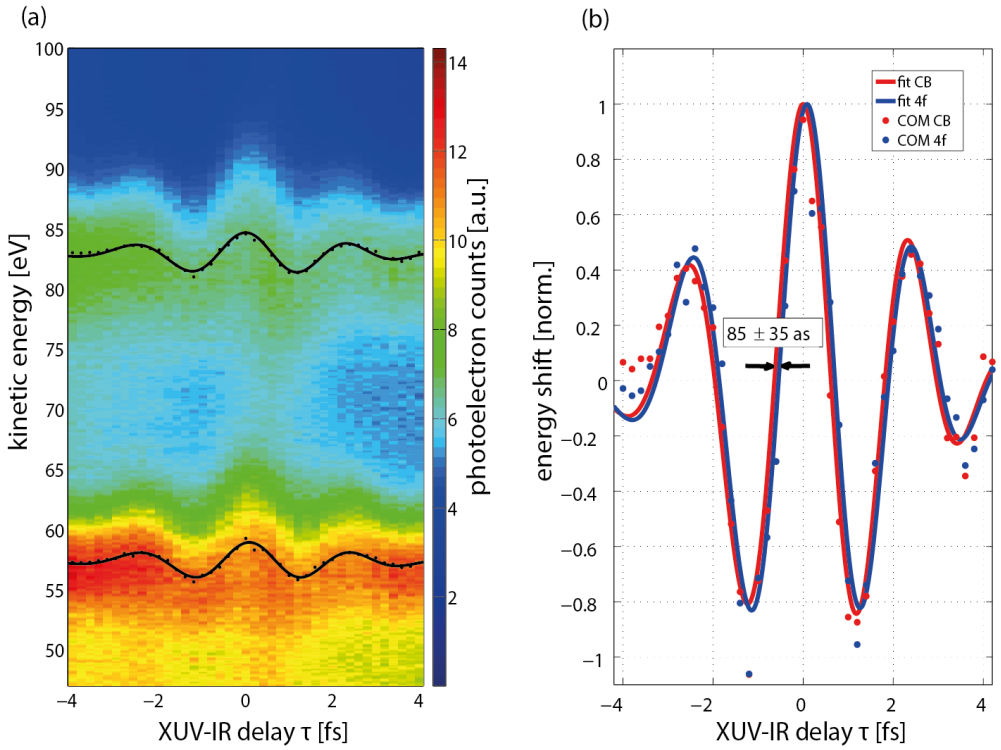

Fig. x.17: (a) Raw attosecond streaking technique spectrogram of a tungsten (110) surface. Photoelectron intensities are given in arbitrary units. **(b)** Center-of-mass (COM) analysis of the spectrogram. The COM of both emission lines measured are given as dots, a global fit to both COM traces is shown in solid lines (from[97] with permission of Wiley).

These results demonstrate the technical capability of measuring photon-induced electron release, electron transport through the topmost atomic layers of a solid sample, and emission into the vacuum in real time, with attosecond temporal resolution. Explaining the state-dependent differences of the emission dynamics seen in the streaking experiment is unfortunately a much more challenging task for metal surfaces than for gaseous targets[31].

3.3Theoretical modeling of attosecond photoemission from tungsten

Four different theoretical approaches explaining the dynamics seen in this W(110) experiment have been put forward, all yielding delayed emission between the core and valence

electrons varying from 42 to 110 as. The first theoretical approach by Echenique *et al*., explained the delayed emission of the core electrons by different group velocities of the final states [53]. Assuming the validity of the static band-structure picture, the authors showed that for the photon energy of the experiment (91 eV) the final-state bands of the valence electrons exhibit stronger dispersion than those of the core electrons. As a result, a smaller effective mass, larger group velocity, and more rapid transport were extracted for the valence electrons, explaining the observed timing. As for the theoretical models discussed below, a critical point of this model was the application of the *static* band structure.

Considering this, in a second study Kazansky and Echenique have investigated the relative contributions of final- and initial-state effects on the observed dynamics[80]. In their revised quantum model, they treat core electrons as localized, and valence electrons as completely delocalized. Attenuation by inelastic scattering is taken into account in addition to electron-hole interaction for the inner-shell levels (but not for valence states). The streaking field inside the metal is set to zero. Pseudopotentials obtained for copper are used to model electron transport in tungsten. Calculations based on this one-dimensional theory also reproduce the experimentally obtained results quite well. Compared with the first approach, however, the relative magnitudes of final- and initial-state effects are reversed.

The authors show that different final state energies for core and valence emission contribute only 10 as to the net relative photoemission delay. To understand this, it must be remembered that the initial energies for valence and core states are different; therefore, their final kinetic energies will be different even if absorbing the same XUV photon. However, standardizing the final energy of core emission to match that of valence band emission induces *only* the 10 as to the relative delay mentioned above. As this factor is minor it is largely ignored, and the observed relative delay is

attributed to the contrast in wave-function localization between the core-level and valence-band states.

A third theoretical study by Lemell *et al*., models the attosecond streaking experiment within a classical electron-transport approach[79]. Quantum effects enter this classical calculation via a stochastic force $F_{stoc}(t)$ containing elastic and inelastic scattering with tungsten cores as well as with conduction electrons. Other forces changing the electrons' momenta result from the NIR streaking field, which penetrates ~85 layers of the solid in their model, and from the potential barrier at the surface. Rather detailed assumptions are made concerning the properties of the various involved electronic states. The authors discriminate 5*p* and 4*f* core electrons and 5*d* and 6*s* valence electrons, and treat only the 6*s* band as delocalized. Elastic scattering cross sections, used as input for the classical calculation, are calculated with the ELSEPA package [103]. Inelastic scattering cross sections and angular distributions of inelastically scattered electrons are obtained from the momentum distribution and energy-dependent dielectric constant of tungsten. Two limiting cases are considered for the final states: (i) A free-particle dispersion relation, and (ii) the group-velocity distribution (cf. supplementary material in[53]). Depending on these two alternatives, emission of the core electrons is found to be delayed from 42 as (case i) to 110 as (case ii). The authors point out, however, that the group-velocity distribution from[81] had to be blue-shifted by 8 eV to obtain the maximum effect. For the limiting case (i), the larger emission depth of core electrons and inelastic scattering of valence electrons (which enter into the energy region of the core photoelectrons) are the main sources of the observed delay. This occurs as these electrons require additional time to escape, again due to inelastic scattering. These electrons are missing in the valence streaking trace, but are included in the core streaking trace. We note that the authors address possible extensions of their model, particularly the inclusion of local field enhancements

at the surface (due to plasmon excitation), which might affect emission and transport of localized and delocalized states differently (cf., Section 4 below).

Here, we will detail the fourth, quantum-mechanical study by Zhang and Thumm[4,5], since the main characteristics of streaked photoemission from solid metal surfaces can be understood within a quantum mechanical, one-active-electron model that includes simplifying assumptions. Compared to[80], the authors include the streaking field inside the solid. They argue that the skin depth (~100 Å) is much larger than the electrons' mean-free path, λ (~5 Å). The precise value of the skin depth is then irrelevant, since photoelectrons originating at a distance from the surface of more than a few times λ do not contribute noticeably to the measured photocurrent. The interaction of the photoelectron with the streaking IR field is treated non-perturbatively, and the photoemission by the XUV pulse is treated in first-order perturbation theory. The initial states are assumed as fully localized core and fully delocalized valence electrons. Core-level photoelectrons from different lattice layers are added coherently to the photoemission yield. Within this model, the interference between photoelectron emissions from 4*f* core levels (that are localized in different lattice planes parallel to the surface) is the main source of the delay. For this relative delay between core-level and CB emission they obtain 110 as, a value compatible with the experiment.

Apart from restricting the electron dynamics to one active electron, simplifying assumptions in the model of Zhang and Thumm[4,5] are included in their representation of (i), the initial state of the active electron, (ii) the propagation of the released photoelectron into the bulk and near the surface, and (iii) the final photoelectron states in terms of a modified Volkov wave (x.29). To further simplify the discussion and remain consistent with the numerical modeling[4,5,78,88,92,96,104] of recently performed experiments on tungsten[53], platinum[105], rhenium[97],

and magnesium[54] surfaces, the assume linearly polarized, grazingly incident XUV and IR pulses with electric field vectors that may be approximated as being perpendicular to the surface.

Due to the large XUV photon energy, XUV photoemission by one or several XUV photons can easily be distinguished in streaked photoelectron spectra. As for the description of photoelectron wave packets in Section 2, we therefore accurately model XUV photo absorption in first order perturbation theory. The transition amplitude for absorption of a single XUV photon resulting in the emission of an electron from an initial Bloch state, $|\Psi_{\vec{k}}(t)>=|\Psi_{\vec{k}}>e^{-i\varepsilon_{\vec{k}}t}$, with crystal momentum $\vec{k}$, and energy $\varepsilon_{\vec{k}}$, of a metal substrate to an IR-field-dressed final continuum state, $|\Psi_f>$, is then given by[4,5]

$$T_{\vec{k}}=-i\int_{-\infty}^{+\infty}dt\,\langle\Psi_f\left|\vec{r}\cdot\vec{E}_X(t+\tau)\right|\Psi_{\vec{k}}\rangle. \qquad \text{(x.42)}$$

As mentioned earlier, the most elementary quantum-mechanical description of photoelectrons is achieved in the SFA, which represents the interaction of the photo-released electron with the IR streaking field by a Volkov final-state wave function (x.29). Including elastic and inelastic scattering of the photo-released electron before its emission from the surface (in terms of the damping factor $e^{\kappa z}$),the final photoemission state is represented as a Volkov wave that is exponentially damped inside the surface[4,5,78],

$$\Psi_f(\vec{r},t)=(2\pi)^{-3/2}e^{i[\vec{k}_f+\vec{A}_{IR}(t)]\cdot\vec{r}+i\Phi_{\vec{k}_f}(t)}[\Theta(z)-\Theta(-z)e^{\kappa z}], \qquad \text{(x.43)}$$

with the Volkov phase [cf. Eq. (x.30)]

$$\Phi_{\vec{k}_f}(t) = -\frac{1}{2}\int^{t} dt' \left[\vec{k}_f + \vec{A}_{IR}(t')\right]^2 \qquad \text{(x.44)}$$

and the unit step function $\Theta(z)$. In this model, all propagation effects that the electron encounters inside the substrate are included in the finite mean-free path$\lambda = 1/(2\kappa)$ [2,98]. Integration of (x.42) over all momenta $\vec{k}$ in the first Brillouin zone [2] yields the photoemission probability

$$P(\vec{k}_f, \tau) = \int_{\vec{k}\epsilon 1.BZ} d\,\vec{k} |\mathrm{T}_{\vec{k}}(\tau)|^2. \qquad \text{(x.45)}$$

The initial state $|\Psi_{\vec{k}}>$in (x.42) is composed of Bloch waves, $|\Psi_{\overrightarrow{k^-}}>$and $|\Psi_{\overrightarrow{k^+}}>$, for electrons moving with (crystal) momenta $\overrightarrow{k^{\pm}} = (\vec{k}, \pm k_z)$) inside the solid towards and away from the surface, respectively, and a transmitted wave[4,5,78]. The transmitted wave decays exponentially into the vacuum ($z > 0$) and is negligible in the applications discussed below. For photoemission from core levels, the Bloch waves are linear superpositions of tightly bound atomic levels, $|\Psi_C>$, that are localized at the lattice points, $\vec{R}_j$, of the substrate. In an elementary approach the atomic core levels can be approximated by closed-form expressions (e.g., screened hydrogenic wave functions), and adjusted to the core level energies ε_B, of the substrate,

$$\Psi_{\vec{k}}{}^{\pm}(\vec{r}, t) = e^{-i\epsilon_B t} \sum_j e^{i\overrightarrow{k^{\pm}}\vec{R}_j} \Psi_C(\vec{r} - \vec{R}_j). \qquad \text{(x.46)}$$

Thus, the corresponding transition amplitude includes the interlayer interference effects, mentioned earlier, in terms of a coherent sum over contributions to the photocurrent from different substrate layers. The relevant layers are located within a distance equal to a small multiple of λ from the surface. In the numerical applications shown below, we model $|\Psi_C>$ by adjusting hydrogenic ground-state orbitals to the core-level binding energy [4,5].

In general, the representation of the initial states in terms of Bloch waves (x.46) can be applied to localized core levels and delocalized valence and conduction-band (CB) states of the substrate. Assuming fully delocalized CB states, an alternative and technically convenient approach consists in representing the substrate's CB with the so-called 'jellium' approximation[98,106]. In the jellium model, electronic motion in the initial states is regarded as free, while the active electron's motion (perpendicular to the surface) is described in terms of eigenfunctions

$$\Psi_{\vec{k}}(\vec{r},z,t) \sim e^{-i\varepsilon_{\vec{k}}t} e^{-i\vec{k}\,\vec{r}}\,(e^{ik_z z} + Re^{-ik_z z}) \qquad \text{(x.47)}$$

of the step potential $U(x,y,z) = -U_0\Theta(z)$, with $U_0 = \varepsilon_F + W$ U, Fermi energy ε_F, work function W, and reflection coefficient $R(U_0,k_z)$. The photoemission yield in the jellium approximation is obtained by replacing the integrals in (x.45) with an integral over the Fermi volume (containing all initially occupied CB states).

3.4 Modeling of the photoemission delay in tungsten

XUV pulses can release electrons from either bound core levels or delocalized conduction band states of a metal surface. The released photoelectrons get exposed to (and 'streaked') by the same

IR probe pulse used to generate the XUV pulse via harmonic generation [32,57]. The two laser pulses are thus synchronized. By varying their delay, τ, Cavalieri *et al.*[53] measured time-resolved, photoelectron kinetic energy distribution $P(\varepsilon_f, \tau)$and deduced a relative delay of 110±70 as between the detection of photoelectrons emitted from 4*f*-core and CB levels of a W(110) surface by absorption of a single XUV photon (Fig. x.18, left column; see also Figs. x.15 and x.17)

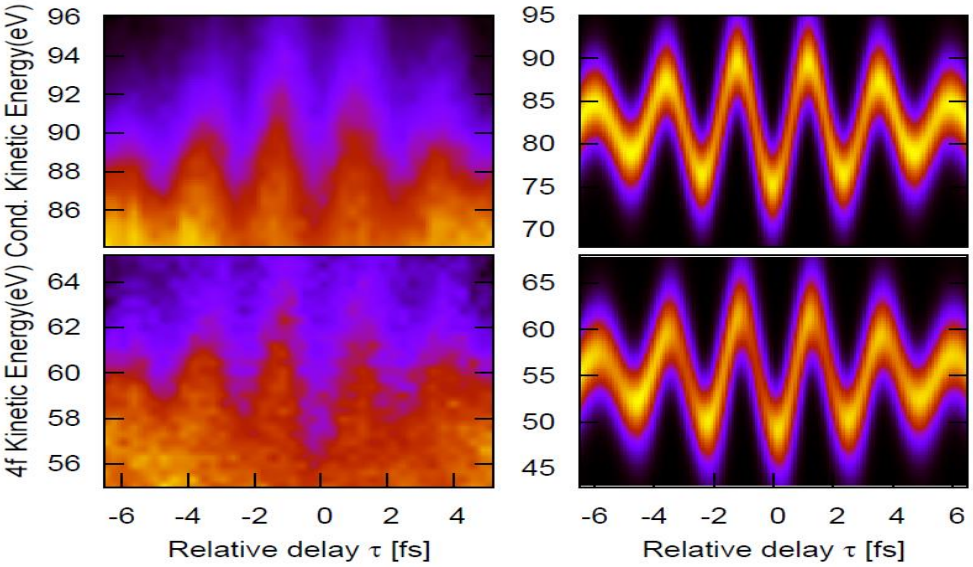

Fig. x.18: Time-resolved, streaked photoelectron spectra for emission from the CB (top) and 4*f*-core levels (bottom) of a W(110) surface as a function of the delay between the XUV and IR pulses. Linear color scales. Experimental results of Cavalieri *et al.* [53](left) in comparison with numerical simulations of Refs.[4] (right). Reprinted with permissions of APS.

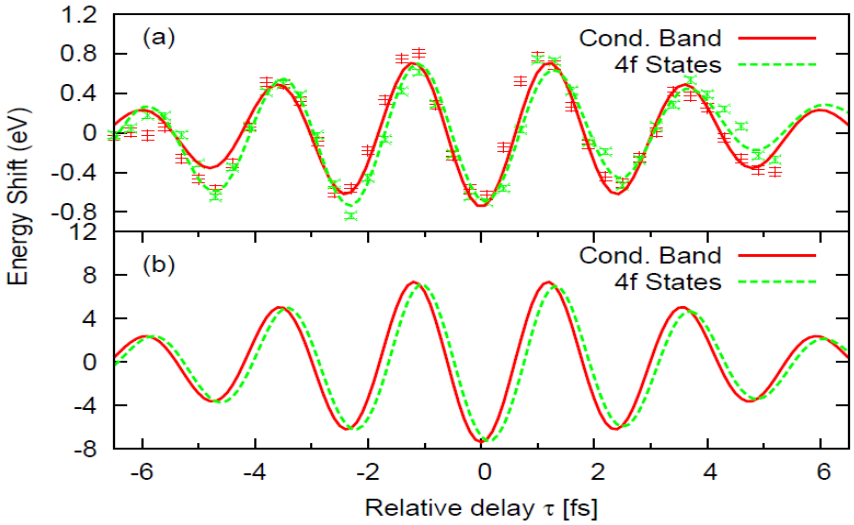

Fig. x.19: Streaked electron spectra for photoemission from CB and 4*f*-core levels of a W(110) surface. **(a)** Measured center-of-energy shifts as a function of the delay between the XUV and IR pulses. The damped sinusoidal curves are fits to the raw experimental data (points with error bars) and are shifted by a relative photoemission time delay of 110±70 as. Adapted from Ref. [53]. **(b)** Calculated center-of-energy shifts showing a relative photoemission time delay of 110 as between the two groups of electrons. The central energy shifts for the 4*f* photoelectrons are multiplied by 2.5 in **(a)** and 1.1 in **(b)**. Adapted from Ref.[4].

To compare these model calculations with this streaking experiment, IR and XUV pulses with Gaussian envelopes are assumed and the experimental parameters of Ref.[53] for IR and XUV pulse lengths (τ_{IR} =6.5fs and τ_X = 0.29 fs [FWHM]), photon energies ($\hbar\omega_{IR}$ = 1.7 eV and $\hbar\omega_X$ = 91 eV), and IR peak intensity (2×10^{12} W/cm^2) are used. For the W(110) surface, measured values for the work function and Fermi energy are 5.5 eV and ε_F =4.5eV, respectively, and the lattice constant in direction perpendicular to the surface is 3.13 Å. Figures x.18 and x.19 show that the simulated modulation of the photoelectron kinetic energy agrees with the measurement. In order to find the relative photoemission delay between the two calculated spectra in the right column of Fig x.18, it is important to compute the center of energies (first moments in energy) in the calculated spectra for the same spectral intervals for which the central energies were deduced from the measured spectra (Fig. x.19). The relative photoemission delay $\Delta t_{X,4f-CB}$between the 4*f*-core level and the CB photoelectrons corresponds to the temporal shift between the two calculated centers of energy in Fig. x.19(b). It agrees well with the experiment for an adjusted electron-mean-free path of λ = 2.65 Å[4,5,98].

3.5 Attosecond photoemission from rhenium surfaces

The time delay measured in the first proof-of-principle experiment with ~300-attosecond XUV pulses centered near 90 eV has a comparably large experimental uncertainty[53]. The accuracy with which such time shifts can be extracted from a streaking spectrogram depends mainly on the depth of the NIR-induced modulation in the photoelectron spectra, the energetic separation between the

photoemission lines (whose emission timing should be analyzed), and the signal-to-noise (S/N) ratio of the photoelectron spectra. Experimentally, the modulation depth can be controlled by the NIR field intensity which, however, has to be restricted to much lower values compared to gas-phase experiments in order to avoid an excessive background signal due to above-threshold photoemission (ATP) electrons. ATP stems from the CB electrons of the solid and is generated by the absorption of multiple NIR photons from the streaking field. To enable an unambiguous analysis of the streaked electron distributions, this background should not overlap with the XUV-induced photoemission lines. In this respect, the use of higher XUV photon energies is beneficial.

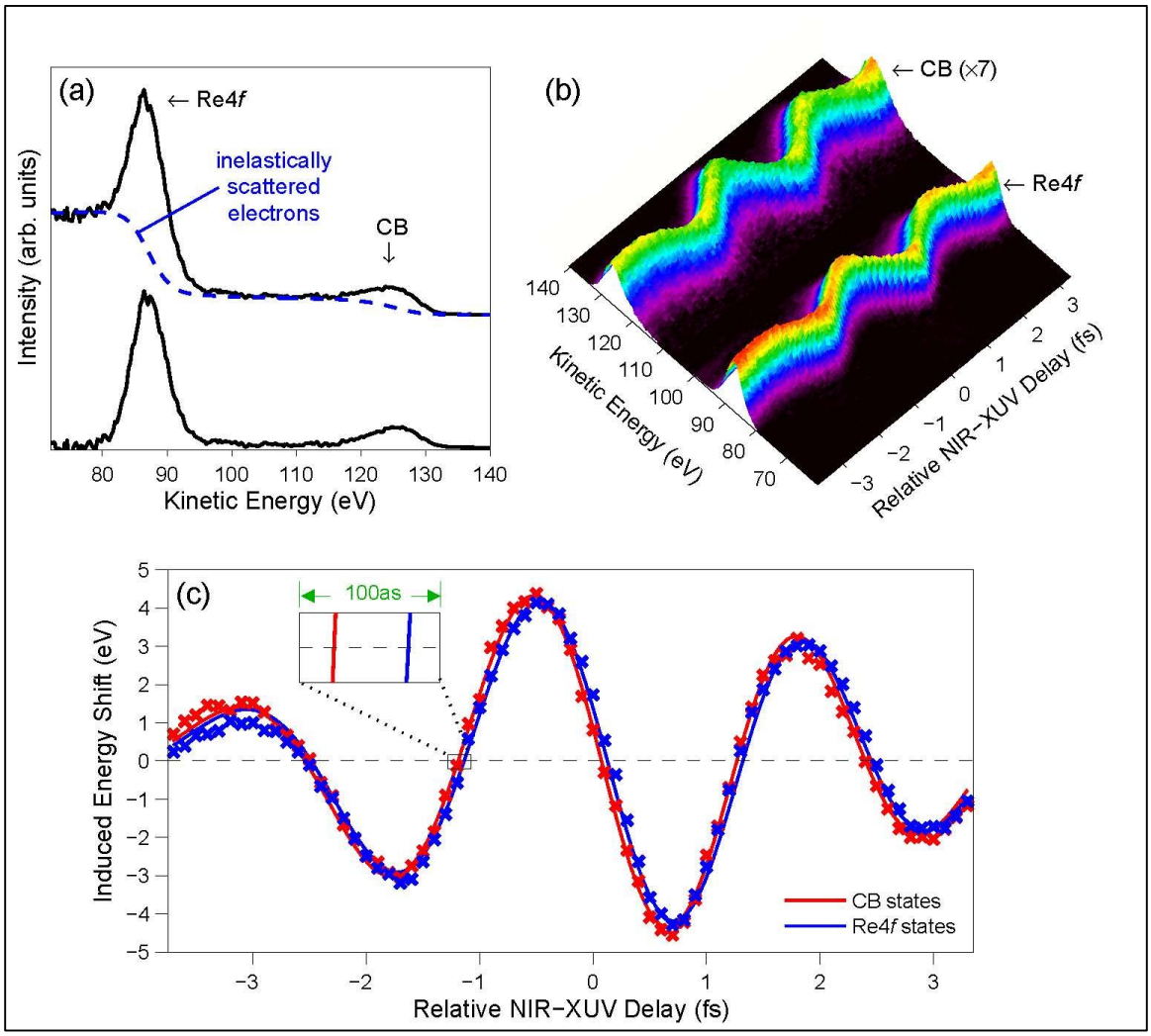

Fig. x.20: Attosecond, time-resolved photoemission from the (0001) surface of rhenium. **(a)** Static photoelectron emission from rhenium (in the absence of the NIR streaking field) obtained with HH radiation filtered by a 6-eV (FWHM) bandwidth mirror centered near 125 eV. The background of inelastically scattered electrons (blue dashed line) is removed before the analysis. The full streaking spectrogram is shown in panel **(b)**, with the CB intensity scaled by a factor of 7. The comparison of the first moments of the streaked electron distributions as a function of the NIR-XUV delay, shown in panel **(c)**, reveals emission of the 4*f* photoelectrons from the metal surface delayed by 100 as compared to the photoelectrons released from the conduction-band states. Adapted from Ref [97].

Fig. x.20(a) shows the photoemission spectrum obtained from the (0001) surface of rhenium with ~350-attosecond XUV pulses with a central photon energy of 125eV. Two emission lines corresponding to the *4f* and the CB states are well resolved, but are superimposed by a background originating from inelastically scattered XUV photoelectrons. This background (blue dashed line) has to be subtracted from the spectra prior to the analysis, which represents a further complication

compared to gas-phase streaking experiments. A background-corrected spectrogram obtained with a 4×10^{11} W/cm^2 NIR dressing field is depicted in panel (b). The results of the data evaluation are shown as crosses in panel (c), along with a global fit of both traces to the same parameterized NIR-waveform (shown as solid lines). A relative shift of 100 as of the 4*f* trace to positive NIR-XUV delays is clearly discernible and reveals the delayed emission of the 4*f* electrons with respect to the CB electrons.

3.6 Attosecond photoemission from magnesium surfaces

Neppl *et al*.[54] measured the relative time delay in the emission of VB and core-level electrons from Mg(0001) surfaces. Mg as a test material is well suited to discern the possible effects of the delay in photoemission since the band structure for this material is "free-electron-like." The influence of the group velocity of the photoelectron wave packet on the photoemission delay can thus be calculated and accounted for. In Fig x.21 shows the streaking spectrograms for both types of electrons. There is no measureable delay in the streaking traces, which indicates that the two types of electrons leave the surface at the same instant. A simple estimation of the respective "travel time" using free-particle velocities and calculated penetration depths[54] shows that the vanishing time delay can be well accounted for by simply considering transport effects – hinting at a negligible contribution from other phenomena, such as initial-state effects.

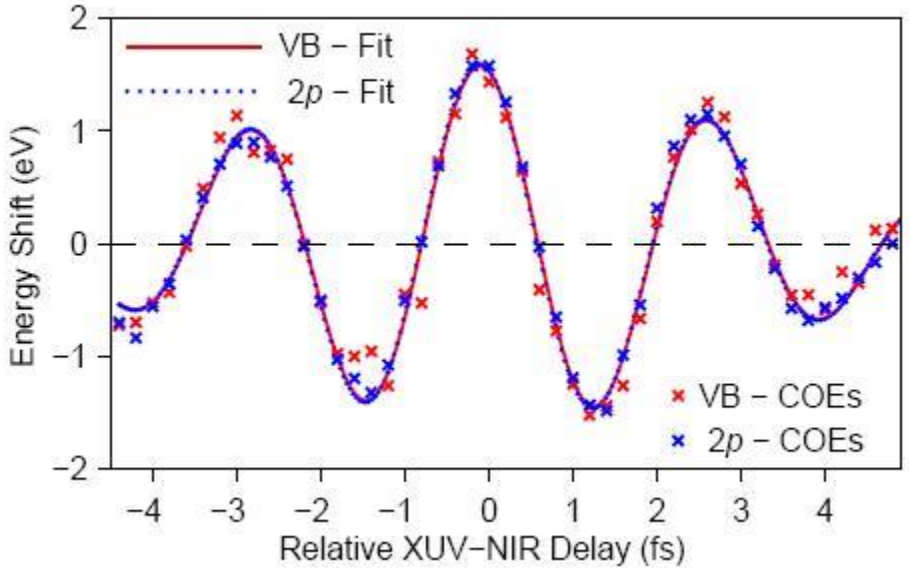

Fig. x.21: Timing analysis of the VB and 2*p* core-level photoemission from Mg(0001). Calculated center-of-energies (COE) for the VB and 2*p* region of the spectrogram (depicted as crosses) are fitted to a pair of parameterized analytic functions describing the vector potential of the NIR streaking pulse. The absence of a relative shift between the fitted functions, shown as red solid line for the VB and blue dotted line for the 2*p* emission, provides evidence for a synchronous release of these electrons from the metal surface. Adapted from Ref [54].

Numerical results for streaked photoemission from Mg(0001) are shown in Fig. x.22. The calculations were performed within a quantum mechanical model[104] similar to the one discussed in Section 3.3,and with the IR laser and XUV parameters of the experiment [54]. In contrast to the model in Section 3.3, the VB of Mg(0001) is modeled by a more realistic potential, (the Chulkov potential[107]). Additionally, the 2*p*-core level is represented by combining Chulkov and Yukawa potentials[80]. These potentials reproduce the respective band structures at the level of density-functional theory. The intensity of the NIR pulse is assumed to decay exponentially inside the solid with a skin depth of about one lattice constant δ_L=2 Å[80,102]. The energy-dependent electron MFP is also taken into account in the calculations. Electron MFPs are adjusted to reproduce the measured XUV synchrotron photoemission spectrum for VB and vanishing relative photoemission

delays for 2p-core level emission. The resultant MFP values are 4.1 Å for VB photoelectrons and 2 Å for 2p-core level photoelectrons, complying with previously published data[2,54,108].

Fig. x.22(a) shows the calculated streaking traces for core level and VB emission. The spectral profile of the photoelectron wave packet and its variation as a function of τ in Fig. x.22(a) are, in general, determined by the spectral profile of the XUV pulse and the dipole matrix element, as detailed in Section 2 above. Surprisingly, the spectrograms exhibit distinct τ-dependent dispersion. The 2*p*-core level photoelectron dispersion is found to be dominantly determined by the XUV pulse and robust against MFP variations. In contrast, the VB photoelectron dispersion is found to be primarily determined by the MFP-dependent dipole matrix element. The corresponding COE shifts in Fig. x.22 (b) do not reveal any noticeable relative photoemission delay, in agreement with the experimental results in Fig. x.21.

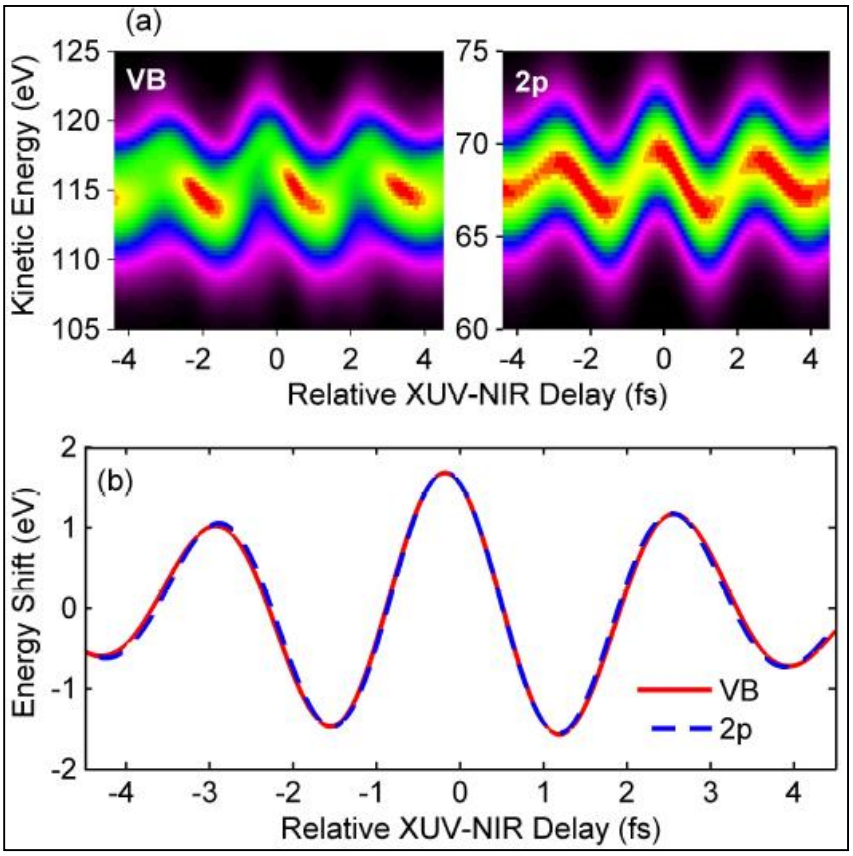

Fig. x.22: **(a)** Calculated streaked photoemission spectrum for a Mg(0001) surface. The XUV-chirp rate is $\beta = -2$ fs^{-2} and the NIR-field CEP is $\phi = 0.78\pi$. The MFPs are $\lambda = 4.1$Å for VB photoelectron and $\lambda = 2$ Å for 2*p*-core level photoelectron. **(b)** Corresponding center-of-energy shift. The VB center-of-energy shift is multiplied by 1.16 for better comparison. Adapted from Ref.[104].

3.7 Towards the time resolution of collective electrons dynamics: Probing plasmon-response effects in streaked photoelectron spectra

Under the correct conditions, the external electromagnetic field can excite modes of collective electron motion where the excited electrons oscillate in unison, so-called plasmons. Plasmons can either be confined to a single nanoparticle (as localized surface plasmons, see Fig. x.23(a)), or propagate along metal-dielectric interfaces (as surface plasmon polaritons, Fig. x.23(b)[109]). In both cases, energy from the external electromagnetic field can be localized below the diffraction limit – to nanometer scales [110]. Some of the spectral properties of plasmons in

nanoparticles – as a function of particle size, shape, and dielectric properties –are reasonably well understood and can be predicted by solving the classical Maxwell equations, including quantum mechanical aspects by appropriate modeling of the particle's dielectric response[111]. These dielectric properties are typically described in terms of phenomenological dielectric response functions that are adjusted to fit measured photoemission and absorption spectra[112,113]. However, the sub-cycle dynamics of collective electronic excitations in strong laser fields (i.e., how such excitations are formed and how their phase coherence is lost) have not been directly measured, and the accurate modeling of the creation and decay of plasmons in nanostructures creates a formidable challenge to theory[109]. The field-free dephasing time of a nanolocalized plasmon is typically in the lower femtosecond domain across the plasmonic spectrum [77].

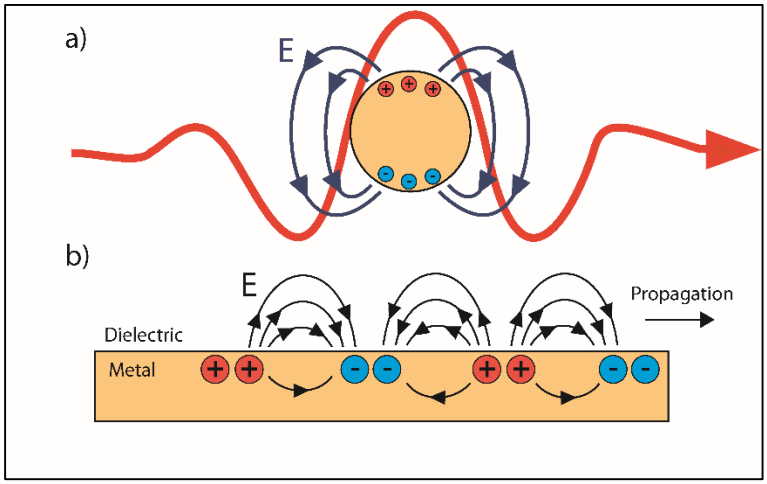

Fig. x.23: Field configurations of **(a)** a localized surface plasmon of a metal nanosphere in an external light field and **(b)** a travelling surface plasmon polariton along a metal-dielectric interface. Adapted from Ref [109].

Photoelectron emission from a metal surface by a sub-femtosecond XUV pulse and the subsequent propagation of those electrons through and near the solid provokes a dielectric response in the substrate that acts back on the electron wave packet[63,114-117] (Fig.x.24). In an attempt to model this many-electron response, a combined classical and quantum mechanical model was suggested[63]. The classical part of this model assumed that the photoelectron moves as a classical

particle at speed v_z, in a direction perpendicular to the surface, corresponding to the charge density $\varrho(\boldsymbol{r},t)=\delta(\boldsymbol{r}_{\parallel})\delta(z-v_z t)$. The response of the solid is described by the complex self-interaction potential

$$\Sigma(z,v_z)=\Sigma_r(z,v_z)+i\Sigma_i(z,v_z), \tag{x.48}$$

which converges for large distances from the surface to the classical image potential $-\frac{1}{4z}$. Its real part, Σ_r, represents an energy shift of the photoelectron by virtual excitations of bulk and surface plasmons and electron-hole pairs in the solid, while its imaginary part, Σ_i, accounts for a loss of photoelectron current due to the interaction between the photoelectron and collective modes of the substrate[63,114]. The electronic self-interactions potential (x.48) is subsequently employed in the quantum-mechanical description of the photoemission process.

The solid is modeled as a wide slab in jellium approximation (see Section 3.3 above), and the time-independent SE is first solved numerically for the potential $V_J(z)+\Sigma_r(z,0)$, with the smeared-out jellium step potential of width a at both sides of the solid-vacuum interface $V_J(z)=-\frac{U_0}{\left\{1+\exp\left(\frac{z}{a}\right)\right\}}$ and the static energy shift $\Sigma_r(z,0)$.[114] This provides the initial bound slab eigenfunctions and their corresponding energies. The effect of the full dielectric response, (x.48), on the released photoelectron wave packet is then accounted for by numerically propagating the TDSE with the potential $V_J(z)+\Sigma(z,v_z)$, and the potentials for the active electron's interaction with the XUV and IR pulses [63].

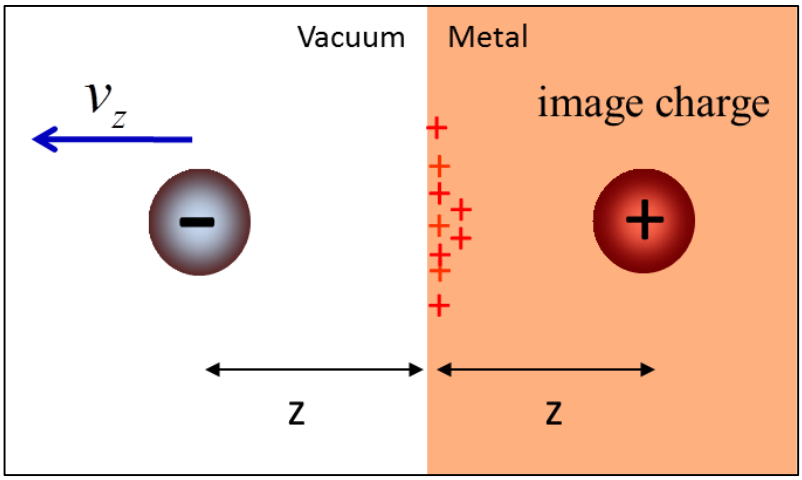

Fig.x.24: A photoelectron held at distance *z* from the surface of a perfect conductor induces a redistribution of the electronic surface-charge density that exerts the same static force on the photoelectron as a fictitious positive image charge inside the substrate. For non-perfect conductors and moving photoelectrons, the self-interaction of the photoelectron deviates from the static image force due to the finite response time of surface and bulk plasmons.

The self-interaction potential $\Sigma(z, v_z)$, can be calculated based on phenomenological dielectric functions, $\varepsilon_B(\boldsymbol{k}, \omega)$ and $\varepsilon_S(\boldsymbol{k}, \omega)$, that model plasmon and particle-hole excitations by the photoelectron in the bulk and at the surface[118,119]. The calculation proceeds analytically by propagating the initial state of the bulk and surface plasmon quantum field, $\Psi(t = 0)$, subject to the interaction $H_{int} = \int d\boldsymbol{r}\, \varrho(\boldsymbol{r}, t)\Psi(\boldsymbol{r}, t = 0)$ [120,121]. This propagation calculation can be mostly carried out analytically and results in a lengthy expression[63] for $\Sigma(t, v_z) = \frac{1}{2} < \Psi(t) \;/ H_{int}(t) \;/ \Psi(t) >$ that depends on the bulk (ω_B)and surface plasmon frequencies ($\omega_S = \omega_B /\sqrt{2}$). Figure x.25 shows streaked photoemission spectra for an aluminum model surface with U_0 = 10.2 eV, ω_S= 0.378, a = 1.4 Å, λ= 5 Å, and δ_L=0, and a 300 as XUV pulse centered at $\hbar\omega_X$= 40 eV. The streaked spectrum in Fig. x.25(a) is calculated by solving the TDSE with the "dynamical" plasmon response $\Sigma(z, v_z)$. As a reference, Fig. x.25(b) shows the photoemission spectrum obtained using the "static" response $\Sigma_r\,(z, 0)$ in the propagation calculation. The central energies for the two

spectra are shifted by the streaking-time-delay difference$\Delta t_{X,wake} = t_{X,\ dyn} - t_{X,\ sta} = 100\ as$ [Fig. x.25(c)].

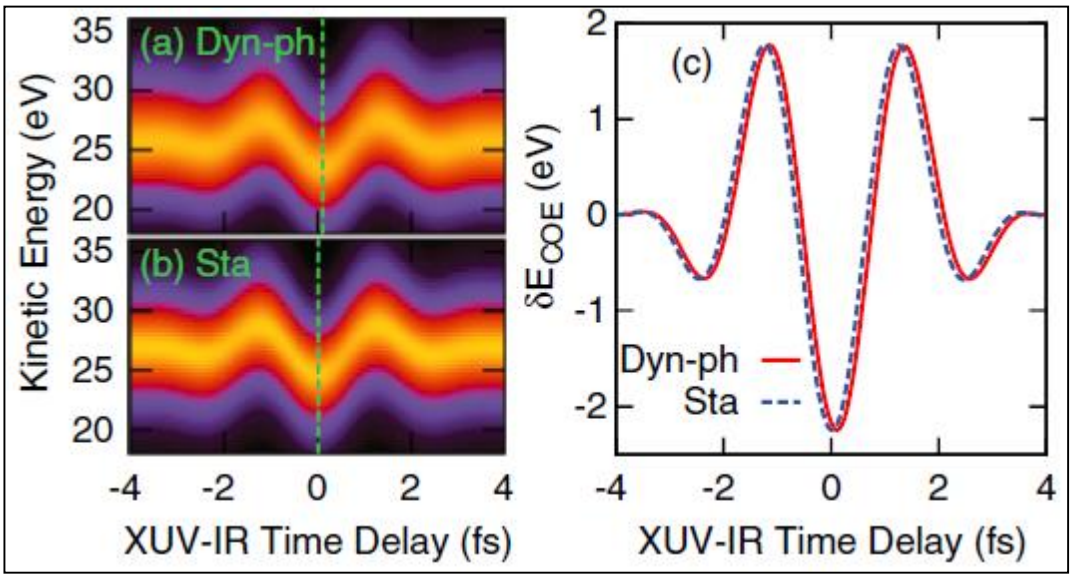

Fig.x.25: Streaked photoelectron spectra as a function of the pump-probe delay for a model aluminum surface and $\hbar\omega_X$ = 40 eV: **(a)** including the dynamical plasmon response duringthe motion of the photoelectron; **(b)** including the plasmon response in static (adiabatic) approximation, allowing the plasmon field an infinite time to adjust to the perturbation by a classical photoelectron at any given position. **(c)** Central energies of the spectra in **(a)** and **(b)** showing a streaking-time-delay difference of 100 as. Adapted from Ref.[63].

Streaking-delay differences, $\Delta t_{X,wake}$ are shown for different mean-free paths in Fig. x.26(a) and for different plasmon frequencies (i.e., electron densities) in Fig. x.26(b) as a function of $\hbar\omega_X$. Figure x.26(a) shows results for the surface-plasmon frequency ω_S= 0.378, Fig. x.26(b) for the MFP λ = 5 Å. All other parameters are as in Fig. x.25. Increasing λ by a factor of two significantly increases $\Delta t_{X,wake}$ for XUV photon energies $\hbar\omega_X$< 50 eV, but has little influence at larger ω_X (Fig. x.26 (a)). The results in Fig. x.26 are incompatible with the interpretation [53,80] of the observed[53] delay between photoemission from core and conduction-band levels in tungsten in terms of the photoelectron's travel time in the solid, $\lambda/< v_z >$.

Decreasing ω_S shifts the double-hump structure to lower ω_X(lower photoelectron energies), as expected in view of the decreased thresholds for plasmon excitations (Fig. x.26 (b)).

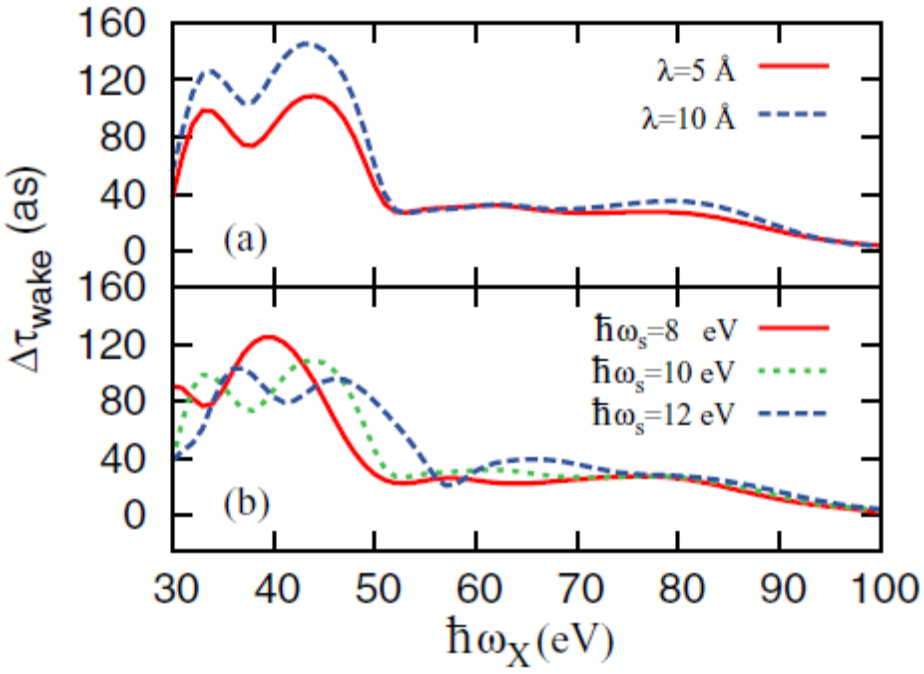

Fig. x.26: Streaking-delay difference $\Delta t_{X,wake}$, induced by the non-adiabatic response of model substrates, as a function of the XUV photon energy for different **(a)** electron mean-free paths λ, and **(b)** surface plasmon frequencies ω_S. Adapted from Ref.[63].

4. Attosecond streaking from nanostructures

The spatial homogeneity of the driving laser field is one of the key aspects in the attosecond streaking of atoms or surfaces[17,31,122]. Nanosystems, in contrast, can exhibit vast spatial variations of local field profiles especially in amplitude and phase. Nanoscopic effects such as field enhancement, resonant (plasmonic) oscillations and coupling of multiple elements is dependent on material properties as well as shape and environment [113]. The spectral composition of the incident radiation gives a certain control over these effects. As nanofabrication technology progresses, ever-increasing control over these properties is gained. The result is custom or tailored materials which can be produced to respond in specific ways to external fields.

Based on theoretical work, in the following we discuss attosecond nanoplasmonic streaking and its application in the measurement of collective electron dynamics within nanostructures in external fields.

4.1 Instantaneous versus ponderomotive streaking

The principle regimes for attosecond streaking from nanostructures were introduced by Stockman *et al.* [67], and will be discussed next for spherical metal nanoparticles. Here we will follow the formalism and presentation in[68,109]. The experimental arrangement, depicted in Fig x.27, is identical to streaking from gases or surfaces as discussed above. The main difference is that a nanostructure (here a single nanoparticle) is the target.

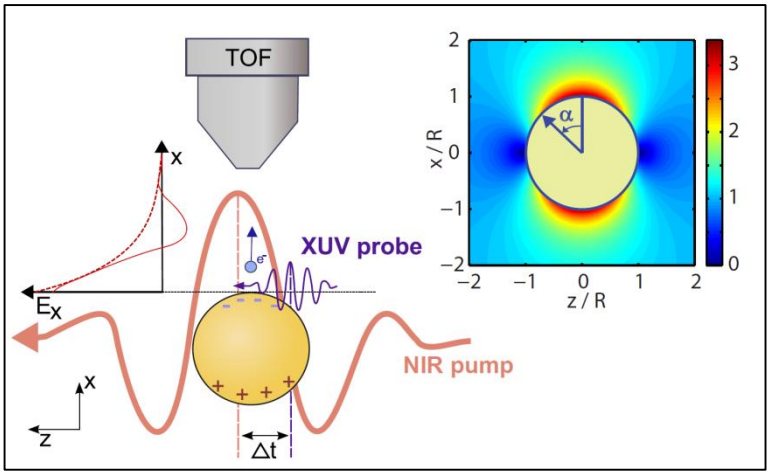

Fig. x.27: Attosecond nanoplasmonic streaking principle illustrated for a spherical metal particle. An NIR pump pulse excites a localized surface plasmon in a metal nanoparticle, and a synchronized attosecond extreme-ultraviolet (XUV) pulse ejects photoelectrons. The field caused by the collective electron motion in the nanoparticle is imprinted in the kinetic energy of the electrons, which are measured by time-of-flight (TOF) spectroscopy. The inset shows the near-field around the nanoparticle as calculated by Mie theory in the y = 0 plane through the center of the sphere[68]. Due to the symmetry of the plasmonic field, the point of electron emission is uniquely defined by the angle α. Reprinted from[68] with copyright permission of APS.

Electrons are emitted by an attosecond XUV pulse which can be synchronized to a driving laser field in the optical region. On their way to the detector, the photoelectrons are accelerated by the

near-field which results in an effective change in their kinetic energy. For more complex nanostructure geometries, the electric near-field may need to be evaluated using numerical computations such as the finite-difference time-domain (FDTD) method[123]. For spherical nanoparticles, Mie theory [124] can be employed. The inset in Fig. x.27 shows the maximum near-field of a Au nanoparticle resulting from the interaction of a few-cycle pulse at 800 nm with a 100nm diameter gold nanosphere[68]. The enhancement of the near-field close the surface of the gold sphere is clearly visible and takes a dipolar shape. The spatial inhomogeneity of this near-field leads to substantial differences in the acceleration of the electrons as compared to streaking in gases or from planar surfaces.

The final drift velocity of a photoelectron emitted from a nanoparticle by an XUV pulse at time t_e with initial velocity $\vec{v}_0$ can be obtained by integrating the electron's classical equation of motion

$$\vec{v}_f(t_e) = \vec{v}_0 - \int_{t_e}^{\infty} \vec{E}(\vec{r},t)dt. \qquad \text{(x.49)}$$

The initial velocity is determined by the spectrum of the attosecond XUV pulse and the material's work function. The kinetic energy of released electrons is then given by the difference between the photon energy and the local work function. It was shown that the evolution of plasmonic near-fields from many simple nanostructured surfaces into free space can be well approximated by an exponential function [125]. Introducing the spatial decay constant χ, the decay of the field component perpendicular to the surface can be written as

$$E(x,t) = E_{pl}(t)\exp\left(\frac{-x(t)}{\chi}\right) \qquad \text{(x.50)}$$

where it is assumed that the surface is normal to the *x*-axis and the electron is emitted in the *x*-direction (towards the TOF detector). Note that χ is not a constant and depends on the emission position from the nanostructure (for a nanosphere given by the angle α in Fig. x.27) and the emission angle of the electron trajectory. The change in the electron's drift velocity by acceleration in the near-field of the nanostructure is typically smaller than the initial velocity v_0. For example, an electron with E_{kin} = 100 eV and a streaking amplitude of 10 eV experiences a relative change in velocity of only $\frac{(v_0+\Delta_v)}{v_0} \approx 5\%$. The electron's distance from the surface can thus be approximated by

$$x(t) \approx x_0 + v_0(t - t_e) \tag{x.51}$$

Inserting $x(t)$ into eq. (x.50) yields

$$E(x,t) = E_{pl}(t)\exp\left(\frac{-v_0(t-t_e)}{\chi}\right) = E_{pl}(t)\exp\left(\frac{-(t-t_e)}{\tau_s}\right) \tag{x.52}$$

where the spatial decay time is defined as $\tau_s = \frac{\chi}{v_0}$. Treating the plasmonic response as a damped, driven oscillator[113] results in an exponential decay of $E_{pl}(t)$ after its excitation at $t = 0$, which may be described by

$$E_{pl}(t) = E_0 \cos(\omega t - \phi_{CEP}) \exp\left(\frac{-t}{\tau_{pl}}\right) \quad \text{(x.53)}$$

where E_0 is the peak field amplitude, ϕ_{CEP} the carrier-envelope phase of the plasmonic field, and $\tau_{pl}$the temporal decay constant. Inserting equations (x.51), (x.52), and (x.53) into (x.49) yields

$$\Delta v(t_e) = v_0 - v(t_e) = -\int_{t_e}^{\infty} E_0 \exp\left(-\frac{t}{\tau_{pl}} - \frac{t - t_e}{\tau_s}\right) \cos(\omega t - \phi_{CEP}) dt \quad \text{(x.54)}$$

With the simplifications made above, Eq. (x.54) can be integrated (for the result see [68]). Note that this equation only holds for probing the field *after* its excitation when the plasmon is decaying. The streaking amplitude will exhibit an exponential decay $\exp(-t_e/\tau_{pl})$ which directly reflects the temporal decay of the near-field. The streaking regime can be characterized by the phase shift $\Delta\phi_s$ between the waveform which is apparent in the streaking spectrogram and the local near-field oscillation (see Fig. x.28(a)),

$$\Delta\phi_s = \arctan\left(\frac{\tau_{pl}\tau_s\omega}{\tau_{pl}+\tau_s}\right). \quad \text{(x.55)}$$

If the plasmonic decay constant is much smaller than the spatial decay constant (due to the motion of the electron in the inhomogeneous field), $\tau_{pl} \ll \tau_s$, the phase shift can be reduced to $\Delta\phi_s \approx \arctan(\tau_{pl}\omega)$. In this case $\Delta\phi_s$ is close to $\pi/2$ for oscillating fields with a period shorter than its envelope $(\omega^{-1}) < \tau_{pl}$,which is the case for few-cycle and longer fields. This regime

resembles conventional streaking, where the streaking energy shift is proportional to the vector potential (see Section 2.2 above). It is referred to as the *ponderomotive regime*.

In the opposite limiting case where $\tau_s \ll \tau_{pl}$ and $\tau_s \ll (\omega^{-1})$, the electron will leave the surface during a fraction of a half-cycle of the laser field. In this case the spatial decay time constant is small compared to both the temporal decay constant and the oscillation period. This results in a phase shift close to zero: $\Delta\phi_s = \arctan(\tau_s\omega) \approx 0$. The measured streaking waveform will thus directly reflect the electric field of the plasmonic oscillation. This regime is referred to as the *instantaneous regime*.

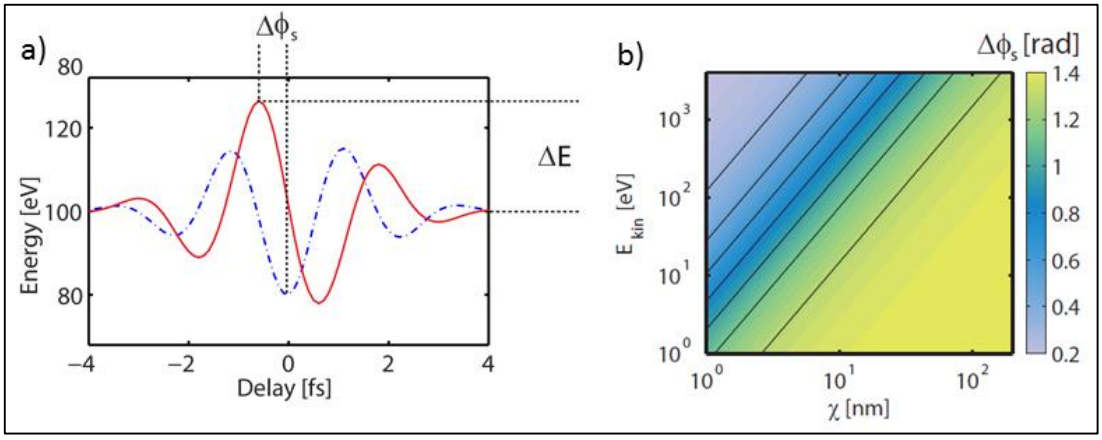

Fig. x.28: (a) Phase shift Δ_s, between the waveform apparent in the streaking spectrogram (red line) and the local near-field oscillation (blue dash-dotted line). **(b)** Phase shift $\Delta\phi_s$as a function of initial electron energy E_{kin} and spatial decay constant χ for a fixed plasmonic decay constant of τ_{pl} = *10* fs and a laser wavelength of λ = 720 nm [109]. The upper left corner ($\Delta\phi_s$ close to zero) corresponds to the instantaneous streaking regime. The lower right corner ($\Delta\phi_s$ close to $\pi/2$) corresponds to the ponderomotive streaking regime.

So far, we have not considered the interaction of near-field-accelerated electrons with the external driving laser field. "Fast" electrons, which leave the near-field within a fraction of an optical period (in the instantaneous regime), are only minimally accelerated by the near-field as compared to ponderomotive streaking in the surrounding external laser field. Under these conditions, the impact of the near-field is determined by its relative strength compared to the driving field, which is simply known as the field-enhancement factor (here denoted as *Q*). The direct field-probing regime

is therefore only achievable with sufficiently high *Q*, present in so-called "hot spots" (with enhancement factors of 2-4 orders of magnitude)[67]. The field enhancement factor and pattern around Au spheres remains similar to the one shown in Fig x.27 (Q≈3) even when decreasing the particle size. For such simple geometries the instantaneous regime cannot be reached and the streaking amplitude is dominated by ponderomotive acceleration in the ambient laser field.

4.2Modeling of the attosecond streaking from metal nanoparticles

To get more insight into the possible outcome of an attosecond nanoplasmonic streaking experiment, numerical simulations have been performed for rectangular Au antennas[66,126] and spherical particles made of both Au[68,126,127] and Ag[128]. The key results from spherical Au particles will be outlined as an example, and special emphasis will be placed on the dependence of the streaking traces on the emission position of the electrons [68].

In the simulations contained in [68], the equations of motion (x.49) were integrated for different emission times t_e, to obtain a complete streaking waveform. The laser field was assumed to have a Gaussian envelope of 5 fs (FWHM of the electric field), a center wavelength of λ = 720 nm, and a peak intensity of 1×10^{12} W/cm^2. The local field was calculated by Mie theory[124], where only the solution for the center wavelength was considered. This is well justified for sizes between 10 nm and 100 nm considered here. The kinetic energy of the electrons after their photoemission was fixed to E_{kin} = 100 eV.

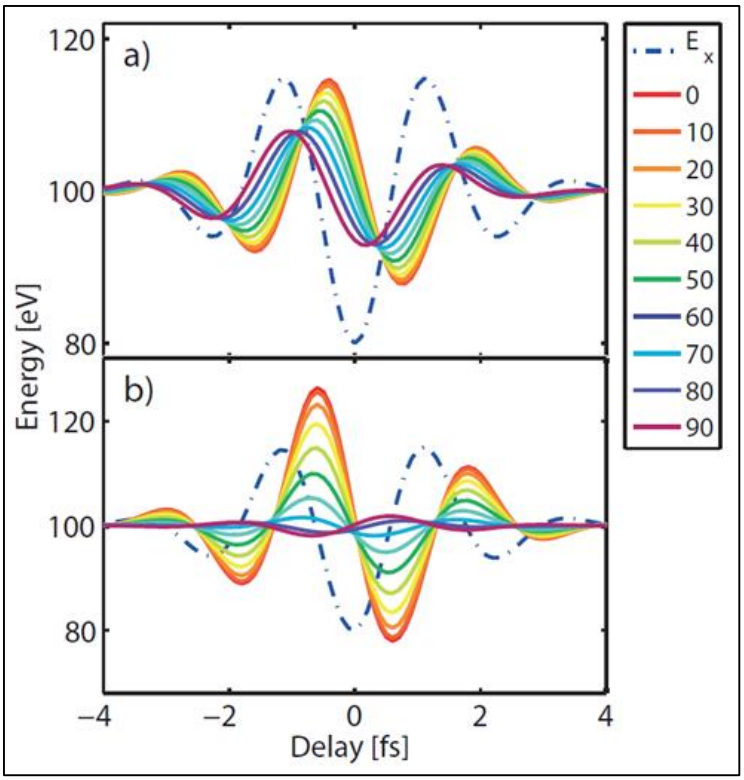

Fig. x.29: Simulated streaking waveforms for electrons emitted at different positions (defined by the angle αin Fig. x.27) on a Au sphere with a diameter of 10 nm **(a)** and 100 nm **(b)**. The blue dash-dotted line indicates the driving field. Adapted from [68] with copyright permission of APS.

Figures x.29 (a) and (b) show simulated streaking curves for different emission positions (defined by the angle α for two different gold spheres, with diameters d = 10 nm and 100 nm, respectively. The driving field is depicted by the blue dashed-dotted line in all plots. For the 10 nm spheres, emission at the pole (α = 0) leads to a phase shift of about 0.3 π with respect to the (negative) driving field. This indicates that the streaking process is in an intermediate regime. Emission at larger angles causes larger phase shifts. For a sphere diameter of 100 nm, the dependence on emission position is even stronger. Here electrons emitted at the pole show a streaking waveform which is phase offset by $\pi/2$ relative to the driving near-field (ponderomotive regime). Going to larger angles α, the streaking amplitude decreases rapidly but only a minor phase shift occurs.

If an experiment does not allow for the discrimination of the emission position (such as with TOF spectroscopy, see Fig. x.27), the attosecond nanoplasmonic streaking spectrogram may contain contributions from all emission positions. The weighting of the contributions from different emission positions depends on the XUV absorption and photoemission. Since typical spot sizes of XUV foci for the photon energy considered here (around 100 eV) are in the micrometer range (much larger than the nanoparticle diameters considered), photoemission will take place over the entire illuminated side of the nanoparticle and, attenuated by the transmission through the material, also on its backside.

Figurex.30 shows streaking spectrograms for 10 nm and 100 nm Au particles that have been computed via Monte-Carlo simulations [68]. The attosecond probe pulse was assigned a pulse length of 250 as, a spectrum centered at 105 eV, and a bandwidth of 7 eV. The emission was assumed to occur from a well-defined, narrow valence band.

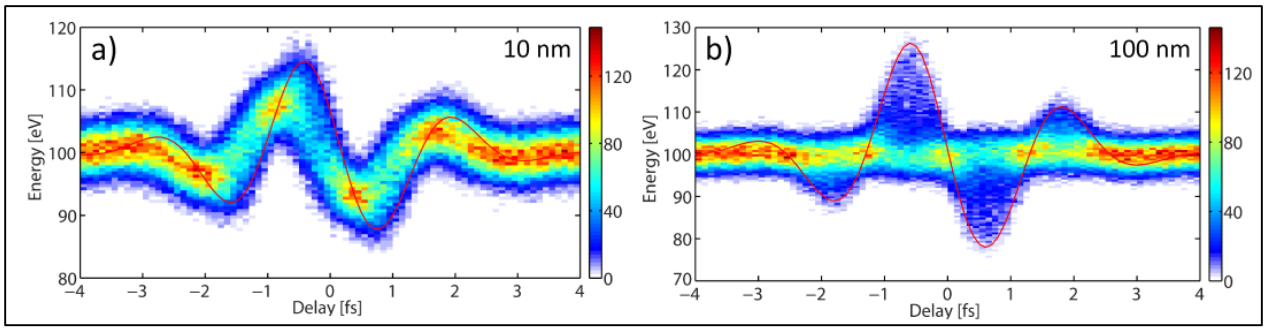

Figx.30: Simulated streaking spectrograms for 10 nm **(a)** and 100 nm **(b)** Au spheres. The red line shows the contribution of electrons emitted on axis with the laser polarization vector. Reprinted from[68] with copyright permission of APS.

The smaller Au sphere exhibits a streaking spectrogram with relatively high contrast and the contributions from different emission positions on the sphere cause a distortion of the waveform. As expected, the spectrogram for the 100 nm sphere is drastically different. The streaking features are blurred and the spectrogram has lost its waveform-like character. The findings are in good

agreement with another study on spherical gold particles[126], where the plasmon decay time was taken into account. In the considered case of a single TOF detector, the streaking spectrograms are not easy to interpret if the system is not well known. Nevertheless, major properties of the plasmonic oscillation can still be recovered. Inspecting Figs.x.29 and x.30, the streaking curves of all trajectories exhibit a crossing at almost the same time for each half-cycle. This results in the characteristic periodic spots in the streaking spectrogram. From the period, one can directly deduce the frequency of the plasmonic oscillation as proposed by Borisov *et al*. [126]. Also the envelope, and thus the lifetime, can be recovered from the spectrogram by analyzing the maximum streaking amplitudes at each delay step. Prell *et al*. proposed using photoelectron angular distributions measured by velocity-map imaging to reconstruct the dipole moment of Ag nanospheres [128].

Similar results were shown for coupled systems on a substrate [66], where the streaking process from the gap region of a coupled antenna was simulated. The results show that due to the high homogeneity of the field enhancement within the gap region, averaging over electron emission positions yields clear streaking spectrograms predominantly in the ponderomotive regime [66].

4.3 Attosecond nanoplasmonic microscopy

Combining the described nanoplasmonic streaking technique with ultrahigh, nanometer spatial resolution is highly desirable for measurements on surface-assembled nanostructures.

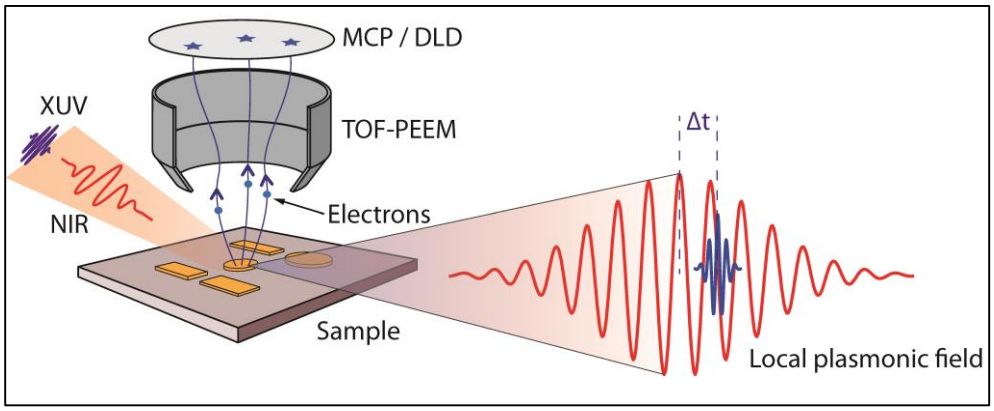

Figure x.31: Principle of the attosecond nanoplasmonic microscope (adapted from Ref. [67]). A short NIR pulse induces plasmonic oscillations which are probed by a time-delayed attosecond XUV pulse. The streaked photoelectrons are imaged with a time-of-flight PEEM (TOF-PEEM), where their time-of-flight and position are detected by a microchannel plate (MCP)/delay-line detector. Streaking spectrograms for each image point can be measured by scanning the delay between the pump and probe pulses.

Stockman *et al*. proposed the combination of photoemission electron microscopy (PEEM) and attosecond nanoplasmonic streaking for the non-invasive, direct probing of nanoplasmonic fields with nanometer (spatial) and attosecond (temporal) resolution[67]. The principle of this technique is shown in Fig x.31. A short, NIR laser pulse excites the collective electron dynamics on a nanostructured surface, then a synchronized attosecond XUV pulse photoemits electrons from the surface. These electrons are then accelerated in the plasmonic near-fields as described in the last section. However, in contrast to conventional streaking spectroscopy, now the detector is a time-of-flight PEEM (TOF-PEEM), which enables the imaging of photoelectrons from the sample surface with nanometer resolution[129]. By scanning the delay between the NIR pump and XUV probe pulses, a streaking spectrogram is obtained for each image point on the TOF-PEEM, representing a small volume on the sample surface.

The theoretical study by Stockman *et al*. included calculations for a rough silver surface with hot spots exhibiting field enhancement factors of $Q = 30$ and a spatial extent of only a few nanometers[67].

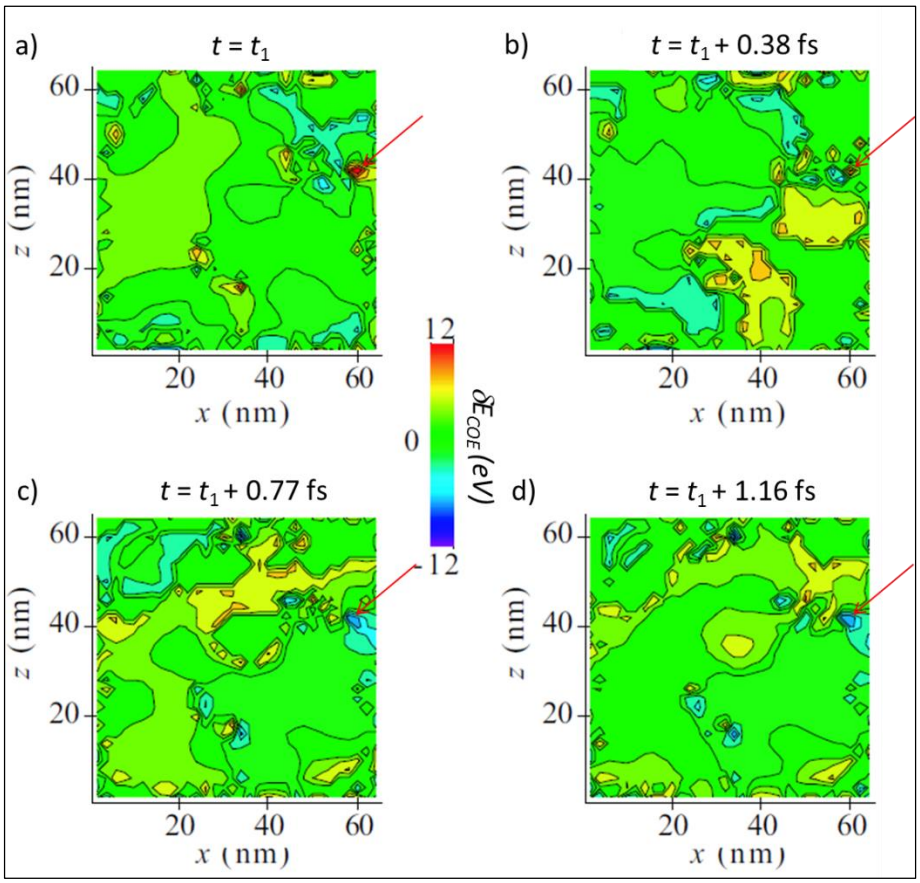

Figure x.32: Topographic color maps of the streaking energy shift δE_{COE}, of electrons emitted by an XUV pulse in the plane of this nanostructure. **(a)-(d)** show different times after excitation of the nanostructure by a 5.5 fs pulse at 800 nm. The time t_1 corresponds to a time at which the near-field in the hotspot (indicated by the red arrow) has reached a peak. Adapted from[67] with copyright permission of Nature.

These hot spots are so small that the electron escape time is much smaller than the plasmonic oscillation period. For this limiting case, a direct mapping of the near-fields in the instantaneous regime is possible.

Results of the calculations by Stockman *et al.* [67] are shown in Fig. x.32. An attosecond XUV pulse at 90 eV with a pulse duration of 170 as was employed. The XUV pulse is synchronized with a few-cycle optical field (5 fs in duration) for the excitation of the nanosystem, and both are focused onto the sample. Due to their large kinetic energy and short emission time,

the XUV-emitted VB photoelectrons escape from the nanometer-sized regions of local electric field enhancement within a fraction of the oscillation period of the driven plasmonic field.

The spatial resolution is limited by the aberrations of the TOF-PEEM electron optics and experimental conditions (such as space-charge generation). Using UV excitation, Lin *et al*. reached 25 nm spatial resolution with a TOF-PEEM[129]. The application of attosecond XUV photoemission in TOF-PEEM and PEEM poses some challenges. These have been outlined in [130,131], but even in those studies resolutions in the few-100-nanometer range have already been realized and will likely improve. The temporal resolution is determined by the duration of the attosecond pulse and the TOF of the photoelectrons through the local-field region. This can be on the order of a few hundred attoseconds. Fig. x.32 shows that streaking amplitudes of up to approxiamtely 10 eV at an NIR intensity of 1×10^{10} W/cm^2 can be achieved for typical experimental parameters[67]. At this intensity of the driving NIR laser pulse, the direct streaking of the electrons by the external NIR field can be neglected. These theoretical studies show that spatio-temporal measurements in the nanometer-attosecond range can be achieved. The full experimental implementation of the attosecond nanoplasmonic field microscope will thus mark an important advancement of attosecond photoelectron spectroscopy and its applications.

Conclusions

In this chapter we reviewed the basic physics behind state-of-the-art investigations of ultrafast electronic dynamics in atoms, solid surfaces, and nanoparticles. We discussed how XUV photoelectron emission can, with the help of a streaking IR laser field, measure time differences between the emission of electrons from two different initial states at the time-scale of the motion of electrons in matter. We further analyzed the influence the streaking electric field has on the

measured observables, XUV-IR-pulse-delay-dependent photoelectron energy distributions (photoelectron dispersion) and photoemission time delays, and provided simple examples to illustrate the effects of initial- and final-state distortions on streaked photoelectron spectra. We discussed recently measured streaking experiments for photoemission from metal surfaces in comparison with theoretical models. For streaked photoemission from nanoscale particles, we explained simulation results that reveal effects due to the significant local electric field enhancement at nanometer-sized "hot spots" near the nanoparticle surface.

Attosecond physics has been rapidly established over the past decade as a promising research direction, to a large part through novel, attosecond time-resolved laser-streaked XUV photoemission spectroscopy of atoms in the gas phase. More recently, over the past few years, attosecond physics has begun to branch out to more complex systems, holding promise to enable, with attosecond resolution in time and (tens of) nanometer spatial resolution, investigations of basic electronic process on (adsorbate-covered) solid surfaces, semiconductor interfaces, nanostructures, large biomolecules.

The extension of attosecond science to include complex systems has the potential to promote the development of diagnostic tools for basic research with atomic-scale resolution in both, space and time, and to lead to novel devices for information processing, drug delivery, and imaging in medicine in material science.

Acknowledgements

We acknowledge countless contributions to the presented work by our coworkers and collaborators at JRML, KSU, MPQ, LMU and TUM. This work was supported by the MPG and the DFG via the excellence cluster 'Munich Center for Advanced Photonics (MAP)' and SPP1391. We acknowledge partial support by the NSF and the Division of Chemical Sciences, Office of Basic Energy Sciences, Office of Energy Research, U.S. Department of Energy.

References

(1) Hertz, H.: Ueber einen Einfluss des ultravioletten Lichtes auf die electrische Entladung. *Annalen der Physik* **1887**, *267*, 983-1000.

(2) Hüfner, S.: *Photoelectron spectroscopy: principles and applications*; 3rd ed.; Springer: Berlin ; New York, 2003.

(3) Einstein, A.: Über einen die Erzeugung und Verwandlung des Lichtes betreffenden heuristischen Gesichtspunkt [AdP 17, 132 (1905)]. *Annalen der Physik* **1905**, *14*, 164-181.

(4) Zhang, C. H.; Thumm, U.: Attosecond Photoelectron Spectroscopy of Metal Surfaces. *Physical Review Letters* **2009**, *102*, 123601.

(5) Zhang, C. H.; Thumm, U.: Erratum: Attosecond Photoelectron Spectroscopy of Metal Surfaces [Phys. Rev. Lett. 102, 123601 (2009)]. *Physical Review Letters* **2009**, *103*, 239902.

(6) Bransden, B. H.; Joachain, C. J.: *Physics of atoms and molecules*; 2nd ed.; Prentice Hall: Harlow, England ; New York, 2003.

(7) Desjonquères, M. C.; Spanjaard, D.: *Concepts in surface physics*; 2nd ed.; Springer: Berlin ; New York, 1996.

(8) Ullrich, J.; Rudenko, A.; Moshammer, R.: Free-electron lasers: new avenues in molecular physics and photochemistry. *Annual Review of Physical Chemistry* **2012**, *63*, 635-60.

(9) Zewail, A. H.: Femtochemistry: Atomic-Scale Dynamics of the Chemical Bond†. *The Journal of Physical Chemistry A* **2000**, *104*, 5660-5694.

(10) Krausz, F.; Ivanov, M.: Attosecond physics. *Rev. Mod. Phys.* **2009**, *81*, 163-234.

(11) Hentschel, M.; Kienberger, R.; Spielmann, C.; Raider, G. A.; Milosevic, N.; Brabec, T.; Corkum, P.; Heinzmann, U.; Drescher, M.; Krausz, F.: Attosecond Metrology. *Nature* **2001**, *414*, 509-513.

(12) Paul, P. M.; Toma, E. S.; Breger, P.; Mullot, G.; Augé, F.; Balcou, P.; Muller, H. G.; Agostini, P.: Observation of a Train of Attosecond Pulses from High Harmonic Generation. *Science* **2001**, *292*, 1689-1692.

(13) Yanovsky, V.; Chvykov, V.; Kalinchenko, G.; Rousseau, P.; Planchon, T.; Matsuoka, T.; Maksimchuk, A.; Nees, J.; Cheriaux, G.; Mourou, G.; Krushelnick, K.: Ultra-high intensity-300-TW laser at 0.1 Hz repetition rate. *Opt. Exp.* **2008**, *16*, 2109-2114.

(14) Zhang, X.; Schneider, E.; Taft, G.; Kapteyn, H.; Murnane, M.; Backus, S.: Multi-microjoule, MHz repetition rate Ti:sapphire ultrafast regenerative amplifier system. *Opt. Exp.* **2012**, *20*, 7015-7021.

(15) Dubietis, A.; Butkus, R.; Piskarskas, A. P.: Trends in Chirped Pulse Optical Parametric Amplification. *IEEE J. Sel. Top. Quant. Electr.* **2006**, *12*, 163.

(16) Chalus, O.; Bates, P. K.; Smolarski, M.; Biegert, J.: Mid-IR short-pulse OPCPA with micro-Joule energy at 100 kHz. *Opt. Exp.* **2009**, *17*, 3587-3594.

(17) Goulielmakis, E.; Schultze, M.; Hofstetter, M.; Yakovlev, V. S.; Gagnon, J.; Uiberacker, M.; Aquila, A. L.; Gullikson, E. M.; Attwood, D. T.; Kienberger, R.; Krausz, F.; Kleineberg, U.: Single-Cycle Nonlinear Optics. *Science* **2008**, *320*, 1614-1617.

(18) Krausz, F.; Ivanov, M.: Attosecond physics. *Reviews of Modern Physics* **2009**, *81*, 163-234.

(19) Zhao, K.; Zhang, Q.; Chini, M.; Wu, Y.; Wang, X.; Chang, Z.: Tailoring a 67 attosecond pulse through advantageous phase-mismatch. *Opt. Lett.* **2012**, *37*, 3891-3893.

(20) CODATA: In *http://physics.nist.gov;* NIST, Ed.

(21) Wirth, A.; Hassan, M. T.; Grguras, I.; Gagnon, J.; Moulet, A.; Luu, T. T.; Pabst, S.; Santra, R.; Alahmed, Z. A.; Azzeer, A. M.; Yakovlev, V. S.; Pervak, V.; Krausz, F.; Goulielmakis, E.: Synthesized light transients. *Science* **2011**, *334*, 195-200.

(22) Goulielmakis, E.; Yakovlev, V. S.; Cavalieri, A. L.; Uiberacker, M.; Pervak, V.; Apolonski, A.; Kienberger, R.; Kleineberg, U.; Krausz, F.: Attosecond Control and Measurement: Lightwave Electronics. *Science* **2007**, *317*, 769-775.

(23) Schiffrin, A.; Paasch-Colberg, T.; Karpowicz, N.; Apalkov, V.; Gerster, D.; Mühlbrandt, S.; Korbman, M.; Reichert, J.; Schultze, M.; Holzner, S.; Barth, J. V.; Kienberger, R.; Ernstorfer, R.; Yakovlev, V. S.; Stockman, M. I.; Krausz, F.: Optical-field-induced current in dielectrics. *Nature* **2013**, *493*, 70-74.

(24) Schultze, M.; Bothschafter, E. M.; Sommer, A.; Holzner, S.; Schweinberger, W.; Fiess, M.; Hofstetter, M.; Kienberger, R.; Apalkov, V.; Yakovlev, V. S.; Stockman, M. I.; Krausz, F.: Controlling dielectrics with the electric field of light. *Nature* **2013**, *493*, 75-78.

(25) Baltuska, A.; Udem, T.; Uiberacker, M.; Hentschel, M.; Goulielmakis, E.; Gohle, C.; Holzwarth, R.; Yakovlev, V. S.; Scrinzi, A.; Hansch, T. W.; Krausz, F.: Attosecond control of electronic processes by intense light fields. *Nature* **2003**, *421*, 611-615.

(26) Rathje, T.; Johnson, N. G.; Möller, M.; Süßmann, F.; Adolph, D.; Kübel, M.; Kienberger, R.; Kling, M. F.; Paulus, G. G.; Sayler, A. M.: Review of attosecond resolved measurement and control via carrier-envelope phase tagging with above-threshold ionization. *J. Phys. B* **2012**, *45*, 074003.

(27) Wittmann, T.; Horvath, B.; Helml, W.; Schätzel, M. G.; Gu, X.; Cavalieri, A. L.; Paulus, G. G.; Kienberger, R.: Single-shot carrier-envelope phase measurement of few-cycle laser pulses. *Nature Phys.* **2009**, *5*, 357-362.

(28) Kling, M. F.; von den Hoff, P.; Znakovskaya, I.; de Vivie-Riedle, R.: (Sub-)femtosecond control of molecular reactions via tailoring the electric field of light. *Phys. Chem. Chem. Phys.* **2013**, *15*, 9448-9467.

(29) Trebino, R.: *Frequency-Resolved Optical Gating: The Measurement of Ultrashort Laser Pulses*; Springer, 2002.

(30) Itatani, J.; Quere, F.; Yudin, G. L.; Ivanov, M. Y.; Krausz, F.; Corkum, P. B.: Attosecond streak camera. *Phys. Rev. Lett.* **2002**, *88*, 173903.

(31) Kienberger, R.; Goulielmakis, E.; Uiberacker, M.; Baltuska, A.; Yakovlev, V. S.; Bammer, F.; Scrinzi, A.; Westerwalbesloh, T.; Kleineberg, U.; Heinzmann, U.; Drescher, M.; Krausz, F.: Atomic transient recorder. *Nature* **2004**, *427*, 817-821.

(32) Corkum, P. B.: Plasma Perspective on Strong-Field Multiphoton Ionization. *Physical Review Letters* **1993**, *71*, 1994-1997.

(33) Lewenstein, M.; Balcou, P.; Ivanov, M. Y.; L'Huillier, A.; Corkum, P. B.: Theory of high-harmonic generation by low-frequency laser fields. *Phys. Rev. A* **1994**, *49*, 2117-2132.

(34) Sansone, G.; Benedetti, E.; Calegari, F.; Vozzi, C.; Avaldi, L.; Flammini, R.; Poletto, L.; Villoresi, P.; Altucci, C.; Velotta, R.; Stagira, S.; De Silvestri, S.; Nisoli, M.: Isolated Single-Cycle Attosecond Pulses. *Science* **2006**, *314*, 443-446.

(35) Sola, I. J.; Mevel, E.; Elouga, L.; Constant, E.; Strelkov, V.; Poletto, L.; Villoresi, P.; Benedetti, E.; Caumes, J. P.; Stagira, S.; Vozzi, C.; Sansone, G.; Nisoli, M.: Controlling attosecond electron dynamics by phase-stabilized polarization gating. *Nature Phys.* **2006**, *2*, 319-322.

(36) Mashiko, H.; Gilbertson, S.; Li, C.; Khan, S. D.; Shakya, M. M.; Moon, E.; Chang, Z.: Double Optical Gating of High-Order Harmonic Generation with Carrier-Envelope Phase Stabilized Lasers. *Phys. Rev. Lett.* **2008**, *100*, 103906.

(37) Popmintchev, T.; Chen, M.-C.; Arpin, P.; Murnane, M. M.; Kapteyn, H. C.: The attosecond nonlinear optics of bright coherent X-ray generation. *Nature Photonics* **2010**, *4*, 822-832.

(38) Smirnova, O.; Mairesse, Y.; Patchkovskii, S.; Dudovich, N.; Villeneuve, D.; Corkum, P.; Ivanov, M. Y.: High harmonic interferometry of multi-electron dynamics in molecules. *Nature* **2009**, *460*, 972-977.

(39) Lock, R. M.; Ramakrishna, S.; Zhou, X.; Kapteyn, H. C.; Murnane, M. M.; Seideman, T.: Extracting Continuum Electron Dynamics from High Harmonic Emission from Molecules. *Phys. Rev. Lett.* **2012**, *108*, 133901.

(40) Li, W.; Zhou, X.; Lock, R.; Patchkovskii, S.; Stolow, A.; Kapteyn, H. C.; Murnane, M. M.: Time-Resolved Dynamics in N_2O_4 Probed Using High Harmonic Generation. *Science* **2008**, *322*, 1207-1211.

(41) Haessler, S.; Caillat, J.; Salieres, P.: Self-probing of molecules with high harmonic generation. *J. Phys. B* **2011**, *44*, 203001.

(42) Kohler, M. C.; Pfeifer, T.; Hatsagortsyan, K. Z.; Keitel, C. H.: Frontiers of atomic high-harmonic generation. In *Advances in Atomic, Molecular and Optical Physics*; Berman, P., Arimondo, E., Lin, C., Eds.; Elsevier, 2012; Vol. 61; pp 159-208.

(43) Ferrari, F.; Calegari, F.; Lucchini, M.; Vozzi, C.; Stagira, S.; Sansone, G.; Nisoli, M.: High-energy isolated attosecond pulses generated by above-saturation few-cycle fields. *Nature Phot.* **2010**, *4*.

(44) Cavalieri, A. L.; Goulielmakis, E.; Horvath, B.; Helml, W.; Schultze, M.; Fieß, M.; Pervak, V.; Veisz, L.; Yakovlev, V. S.; Uiberacker, M.; Apolonski, A.; Krausz, F.; Kienberger, R.: Intense 1.5-cycle near infrared laser waveforms and their use for the generation of ultra-broadband soft-x-ray harmonic continua. *New J. Phys.* **2007**, *9*, 242.

(45) Feng, X.; Gilbertson, S.; Mashiko, H.; Wang, H.; Khan, S. D.; Chini, M.; Wu, Y.; Zhao, K.; Chang, Z.: Generation of Isolated Attosecond Pulses with 20 to 28 Femtosecond Lasers. *Phys. Rev. Lett.* **2009**, *103*, 183901.

(46) Mairesse, Y.; Quere, F.: Frequency-resolved optical gating for complete reconstruction of attosecond bursts. *Phys. Rev. A* **2005**, *71*, 011401(R).

(47) Gagnon, J.; Goulielmakis, E.; Yakovlev, V. S.: The accurate FROG characterization of attosecond pulses from streaking measurements. *Appl. Phys. B* **2008**, *92*, 25-32.

(48) Chini, M.; Gilbertson, S.; Khan, S. D.; Chang, Z.: Characterizing ultrabroadband attosecond lasers. *Opt. Exp.* **2010**, *18*, 13006-13016.

(49) Zhao, K.; Zhang, Q.; Chini, M.; Wu, Y.; Wang, X.; Chang, Z.: Tailoring a 67 attosecond pulse through advantageous phase-mismatch. *Opt. Lett.* **2012**, *37*, 3891-3893.

(50) Kling, M. F.; Vrakking, M. J. J.: Attosecond Electron Dynamics. *Annu. Rev. Phys. Chem.* **2008**, *59*, 463-492.

(51) Corkum, P. B.; Krausz, F.: Attosecond science. *Nature Physics* **2007**, *3*, 381-387.

(52) Goulielmakis, E.; Loh, Z. H.; Wirth, A.; Santra, R.; Rohringer, N.; Yakovlev, V. S.; Zherebtsov, S.; Pfeifer, T.; Azzeer, A. M.; Kling, M. F.; Leone, S. R.; Krausz, F.: Real-time observation of valence electron motion. *Nature* **2010**, *466*, 739-743.

(53) Cavalieri, A. L.; Muller, N.; Uphues, T.; Yakovlev, V. S.; Baltuska, A.; Horvath, B.; Schmidt, B.; Blumel, L.; Holzwarth, R.; Hendel, S.; Drescher, M.; Kleineberg, U.; Echenique, P. M.; Kienberger, R.; Krausz, F.; Heinzmann, U.: Attosecond spectroscopy in condensed matter. *Nature* **2007**, *449*, 1029-1032.

(54) Neppl, S.; Ernstorfer, R.; Bothschafter, E. M.; Cavalieri, A. L.; Menzel, D.; Barth, J. V.; Krausz, F.; Kienberger, R.; Feulner, P.: Attosecond time-resolved photoemission from core and valence states of magnesium. *Physical Review Letters* **2012**, *109*, 087401.

(55) Schultze, M.; Fieß, M.; Karpowicz, N.; Gagnon, J.; Korbman, M.; Hofstetter, M.; Neppl, S.; Cavalieri, A. L.; Komninos, Y.; Mercouris, T.; Nicolaides, C. A.; Pazourek, R.; Nagele, S.; Feist, J.; Burgdorfer, J.; Azzeer, A. M.; Ernstorfer, R.; Kienberger, R.; Kleineberg, U.; Goulielmakis, E.; Krausz, F.; Yakovlev, V. S.: Delay in photoemission. *Science* **2010**, *328*, 1658-1662.

(56) Klünder, K.; Dahlström, J. M.; Gisselbrecht, M.; Fordell, T.; Swoboda, M.; Guenot, D.; Johnsson, P.; Caillat, J.; Mauritsson, J.; Maquet, A.; Taieb, R.; L'Huillier, A.: Probing Single-Photon Ionization on the Attosecond Time Scale. *Physical Review Letters* **2011**, *106*, 143002.

(57) Dahlstrom, J. M.; L'Huillier, A.; Maquet, A.: Introduction to attosecond delays in photoionization. *Journal of Physics B: Atomic, Molecular and Optical Physics* **2012**, *45*, 183001.

(58) Schultz, T.; Vrakking, M. J. J.: *Attosecond and XUV Spectroscopy*; Wiley, 2013.

(59) Gallmann, L.; Cirelli, C.; Keller, U.: Attosecond Science: Recent Highlights and Future Trends. *Annu. Rev. Phys. Chem.* **2012**, *63*, 447-469.

(60) Scrinzi, A.; Ivanov, M. Y.; Kienberger, R.; Villeneuve, D. M.: Attosecond physics. *J. Phys. B* **2006**, *39*, R1-R37.

(61) *Attosecond Physics: Attosecond measurement and control of physical systems*; Springer, 2013; Vol. 177.

(62) Chang, Z.: *Fundamentals of attosecond optics*; CRC Press, Taylor and Francis Group, 2011.

(63) Zhang, C. H.; Thumm, U.: Probing dielectric-response effects with attosecond time-resolved streaked photoelectron spectroscopy of metal surfaces. *Physical Review A* **2011**, *84*, 063403.

(64) Gertsvolf, M.; Spanner, M.; Rayner, D. M.; Corkum, P. B.: Demonstration of attosecond ionization dynamics inside transparent solids. *J. Phys. B* **2010**, *43*, 131002.

(65) Mitrofanov, A. V.; Verhoef, A. J.; Serebryannikov, E. E.; Lumeau, J.; Glebov, L.; Zheltikov, A. M.; Baltuska, A.: Optical detection of attosecond ionization induced by a few-cycle laser field in a transparent dielectric material. *Phys. Rev. Lett.* **2011**, *106*, 147401.

(66) Skopalova, E.; Lei, D. Y.; Witting, T.; Arrell, C.; Frank, F.; Sonnefraud, Y.; Maier, S. A.; Tisch, J. W. G.; Marangos, J. P.: Numerical simulation of attosecond nanoplasmonic streaking. *New J. Phys.* **2011**, *13*, 083003.

(67) Stockman, M. I.; Kling, M. F.; Kleineberg, U.; Krausz, F.: Attosecond nanoplasmonic-field microscope. *Nature Photonics* **2007**, *1*, 539-544.

(68) Süßmann, F.; Kling, M. F.: Attosecond nanoplasmonic streaking of localized fields near metal nanospheres. *Phys. Rev. B* **2011**, *84*, 121406(R).

(69) Drescher, M.; Hentschel, M.; Kienberger, R.; Uiberacker, M.; Yakovlev, V. S.; Scrinzi, A.; Westerwalbesloh, T.; Kleineberg, U.; Heinzmann, U.; Krausz, F.: Time-resolved atomic inner-shell spectroscopy. *Nature* **2002**, *419*, 803-807.

(70) Miaja-Avila, L.; Saathoff, G.; Mathias, S.; Yin, J.; La-o-vorakiat, C.; Bauer, M.; Aeschlimann, M.; Murnane, M. M.; Kapteyn, H. C.: Direct Measurement of Core-Level Relaxation Dynamics on a Surface-Adsorbate System. *Phys. Rev. Lett.* **2008**, *101*, 046101.

(71) Moore, L. R.; Lysaght, M. A.; Parker, J. S.; van der Hart, H. W.; Taylor, K. T.: Time delay between photoemission from the 2p and 2s subshells of neon. *Phys. Rev. A* **2011**, *84*, 061404.

(72) Nagele, S.; Pazourek, R.; Feist, J.; Burgdorfer, J.: Time shifts in photoemission from a fully correlated two-electron model system. *Phys. Rev. A* **2012**, *85*, 033401.

(73) Pazourek, R.; Feist, J.; Nagele, S.; Burgdorfer, J.: Attosecond Streaking of Correlated Two-Electron Transitions in Helium. *Phys. Rev. Lett.* **2012**, *108*, 163001.

(74) Kubo, A.; Onda, K.; Petek, H.; Sun, Z. J.; Jung, Y. S.; Kim, H. K.: Femtosecond imaging of surface plasmon dynamics in a nanostructured silver film. *Nano Letters* **2005**, *5*, 1123-1127.

(75) Sukharev, M.; Seideman, T.: Phase and polarization control as a route to plasmonic nanodevices. *Nano Letters* **2006**, *6*, 715-719.

(76) Le, F.; Lwin, N. Z.; Halas, N. J.; Nordlander, P.: Plasmonic interactions between a metallic nanoshell and a thin metallic film. *Phys. Rev. B* **2007**, *76*, 165410.

(77) Stockman, M. I.: Nanoplasmonics: The physics behind the applications. *Physics Today* **2011**, *64*, 39-44.

(78) Zhang, C. H.; Thumm, U.: Laser-assisted photoemission from adsorbate-covered metal surfaces: Time-resolved core-hole relaxation dynamics from sideband profiles. *Phys. Rev. A* **2009**, *80*, 032902.

(79) Lemell, C.; Solleder, B.; Tokesi, K.; Burgdorfer, J.: Simulation of attosecond streaking of electrons emitted from a tungsten surface. *Phys. Rev. A* **2009**, *79*, 062901.

(80) Kazansky, A. K.; Echenique, P. M.: One-Electron Model for the Electronic Response of Metal Surfaces to Subfemtosecond Photoexcitation. *Phys. Rev. Lett.* **2009**, *102*, 177401.

(81) Kheifets, A. S.; Ivanov, I. A.: Delay in Atomic Photoionization. *Phys. Rev. Lett.* **2010**, *105*, 233002.

(82) Zhang, C. H.; Thumm, U.: Electron-ion interaction effects in attosecond time-resolved photoelectron spectra. *Phys. Rev. A* **2010**, *82*, 043405.

(83) Nagele, S.; Pazourek, R.; Feist, J.; Doblhoff-Dier, K.; Lemell, C.; Tokesi, K.; Burgdorfer, J.: Time-resolved photoemission by attosecond streaking: extraction of time information. *J. Phys. B* **2011**, *44*, 081001.

(84) Ivanov, I. A.: Time delay in strong-field photoionization of a hydrogen atom. *Phys. Rev. A* **2011**, *83*, 023421.

(85) Zhang, C. H.; Thumm, U.: Streaking and Wigner time delays in photoemission from atoms and surfaces. *Phys. Rev. A* **2011**, *84*, 033401.

(86) Zhang, C. H.; Thumm, U.: Effect of wave-function localization on the time delay in photoemission from surfaces. *Phys. Rev. A* **2011**, *84*, 065403.

(87) Krasovskii, E. E.: Attosecond spectroscopy of solids: Streaking phase shift due to lattice scattering. *Phys. Rev. B* **2011**, *84*, 195106.

(88) Borisov, A. G.; Sanchez-Portal, D.; Kazansky, A. K.; Echenique, P. M.: Resonant and nonresonant processes in attosecond streaking from metals. *Phys. Rev. B* **2013**, *87*, 121110(R).

(89) Eisenbud, L.: Formal properties of nuclear collisions. Ph D, Princeton University, 1948.

(90) Smith, F. T.: Lifetime Matrix in Collision Theory. *Physical Review* **1960**, *118*, 349-356.

(91) Wigner, E. P.: Lower Limit for the Energy Derivative of the Scattering Phase Shift. *Physical Review* **1955**, *98*, 145-147.

(92) Baggesen, J. C.; Madsen, L. B.: Theory for time-resolved measurements of laser-induced electron emission from metal surfaces. *Phys. Rev. A* **2008**, *78*, 032903.

(93) Friedrich, H.: *Theoretical atomic physics*; 3rd ed.; Springer: Berlin ; New York, 2005.

(94) Smirnova, O.; Spanner, M.; Ivanov, M.: Analytical solutions for strong field-driven atomic and molecular one- and two-electron continua and applications to strong-field problems. *Phys. Rev. A* **2008**, *77*, 033407.

(95) Goldstein, H.; Poole, C. P.; Safko, J. L.: *Classical mechanics*; 3rd ed.; Addison Wesley: San Francisco, 2002.

(96) Bothschafter, E.; Neppl, S.; Kienberger, R.: Few-Femtosecond and Attosecond Electron Dynamics at Surfaces. In *Progress in Ultrafast Intense Laser Science IX*; Yamanouchi, K., Ed.; Springer, 2013; pp 183-211.

(97) Cavalieri, A.; Krausz, F.; Ernstorfer, R.; Kienberger, R.; Feulner, P.; Barth, J.; Menzel, D.: Attosecond Time-Resolved Spectroscopy at Surfaces. In *Dynamics at Solid State Surfaces and Interfaces*; Wiley, 2010; pp 537-553.

(98) Zangwill, A.: *Physics at surfaces*; Cambridge University Press: Cambridge Cambridgeshire ; New York, 1988.

(99) Petek, H.; Ogawa, S.: Femtosecond time-resolved two-photon photoemission studies of electron dynamics in metals. *Progress in Surface Science* **1997**, *56*, 239-310.

(100) Drescher, M.; Hentschel, M.; Kienberger, R.; Tempea, G.; Spielmann, C.; Raider, G. A.; Corkum, P.; Krausz, F.: X-ray pulses Approaching the Attosecond Frontier. *Science* **2001**, *291*, 1923-1927.

(101) Magerl, E.; Neppl, S.; Cavalieri, A. L.; Bothschafter, E. M.; Stanislawski, M.; Uphues, T.; Hofstetter, M.; Kleineberg, U.; Barth, J. V.; Menzel, D.; Krausz, F.; Ernstorfer, R.; Kienberger, R.; Feulner, P.: A flexible apparatus for attosecond photoelectron spectroscopy of solids and surfaces. *Rev. Sci. Instr.* **2011**, *82*, 063104.

(102) Krasovskii, E. E.; Silkin, V. M.; Nazarov, V. U.; Echenique, P. M.; Chulkov, E. V.: Dielectric screening and band-structure effects in low-energy photoemission. *Phys. Rev. B* **2010**, *82*, 125102.

(103) Salvat, F.; Jablonski, A.; Powell, C. J.: elsepa—Dirac partial-wave calculation of elastic scattering of electrons and positrons by atoms, positive ions and molecules. *Computer Physics Communications* **2005**, *165*, 157-190.

(104) Liao, Q.; Thumm, U.: In Preparation. **2013**.

(105) Miaja-Avila, L.; Lei, C.; Aeschlimann, M.; Gland, J. L.; Murnane, M. M.; Kapteyn, H. C.; Saathoff, G.: Laser-assisted photoelectric effect from surfaces. *Phys. Rev. Lett.* **2006**, *97*, 113604.

(106) Thumm, U.: Theory of Fast Ion Surface Collisions at Grazing-Incidence - Emission of Electrons Due to Capture and Loss to the Continuum. *J. Phys. B* **1992**, *25*, 421-435.

(107) Chulkov, E. V.; Silkin, V. M.; Echenique, P. M.: Image potential states on metal surfaces: binding energies and wave functions. *Surf. Sci.* **1999**, *437*, 330-352.

(108) Tanuma, S.; Powell, C. J.; Penn, D. R.: Calculations of electron inelastic mean free paths. IX. Data for 41 elemental solids over the 50 eV to 30 keV range. *Surface Interface Analysis* **2011**, *43*, 689-713.

(109) Süßmann, F.; Stebbings, S. L.; Zherebtsov, S.; Chew, S. H.; Stockman, M. I.; Rühl, E.; Kleineberg, U.; Fennel, T.; Kling, M. F.: Attosecond electron dynamics in nanostructures. In *Attosecond Physics*; Schultz, T., Vrakking, M. J. J., Eds.; Wiley, 2013.

(110) Gramov, D. K.; Bozhevolnyi, S. I.: Plasmonics beyond the diffraction limit. *Nature Photonics* **2010**, *4*, 83-91.

(111) Varin, C.; Peltz, C.; Brabec, T.; Fennel, T.: Attosecond plasma wave dynamics in laser-driven cluster nanoplasmas. *Phys. Rev. Lett.* **2012**, *108*, 175007.

(112) Bohren, C.; Huffman, D. R.: *Absorption and scattering of light by small particles*; Wiley: New York, 1983.

(113) Maier, S.: *Plasmonics: fundamentals and applications*; Springer: New York, 2007.

(114) Kurpick, P.; Thumm, U.; Wille, U.: Resonance formation of hydrogenic levels in front of metal surfaces. *Phys. Rev. A* **1997**, *56*, 543-554.

(115) Ducree, J.; Andra, H. J.; Thumm, U.: Neutralization of hyperthermal multiply charged ions at surfaces: Comparison between the extended dynamical overbarrier model and experiment. *Phys. Rev. A* **1999**, *60*, 3029-3043.

(116) Schmitz, A.; Shaw, J.; Chakraborty, H. S.; Thumm, U.: Band-gap-confinement and image-state-recapture effects in the survival of anions scattered from metal surfaces. *Phys. Rev. A* **2010**, *81*, 042901.

(117) Obreshkov, B.; Thumm, U.: H- formation in collisions of hydrogen atoms with an Al(100) surfaces. *Phys. Rev. A* **2013**, *87*, 022903.

(118) García de Abajo, F. J.; Echenique, P. M.: Wake Potential in the Vicinity of a Surface. *Phys. Rev. B* **1992**, *46*, 2663-2675.

(119) García de Abajo, F. J.; Echenique, P. M.: Surface wake in the random-phase approximation. *Physical Review B* **1993**, *48*, 13399-13407.

(120) Gersten, J. I.; Tzoar, N.: Many-Body Formalism for Photoemission Studies. *Phys. Rev. B* **1973**, *8*, 5671-5683.

(121) Tzoar, N.; Gersten, J. I.: Calculation of Many-Body Effects on Energy-Distribution Curves in Photoemission. *Phys. Rev. B* **1973**, *8*, 5684-5695.

(122) Goulielmakis, E.; Uiberacker, M.; Kienberger, R.; Baltuska, A.; Yakovlev, V. S.; Scrinzi, A.; Westerwalbesloh, T.; Kleineberg, U.; Heinzmann, U.; Drescher, M.; Krausz, F.: Direct Measurement of Light Waves. *Science* **2004**, *305*, 1267-1269.

(123) Taflove, A.; Hagness, S. C.: *Computational electrodynamics: the finite-difference time-domain method*; 3 ed.; Artech House: Boston, 2005.

(124) Mie, G.: Beiträge zur Optik trüber Medien, speziell kollodialer Metallösungen. *Ann. Phys.* **1908**, *330*, 337-445.

(125) Lal, S.; Grady, N. K.; Goodrich, G. P.; Halas, N. J.: Profiling the Near Field of a Plasmonic Nanoparticle with Raman-Based Molecular Rulers. *Nano Lett.* **2006**, *6*, 2338-2343.

(126) Borisov, A. G.; Echenique, P. M.; Kazansky, A. K.: Attostreaking with metallic nano-objects. *New J. Phys.* **2012**, *14*, 023036.

(127) Kelkensberg, F.; Koenderink, A. F.; Vrakking, M. J. J.: Attosecond streaking in a nano-plasmonic field. *New J. Phys.* **2012**, *14*, 093034.

(128) Prell, J. S.; Borja, L. J.; Neumark, D. M.; Leone, S. R.: Simulation of attosecond-resolved imaging of the plasmon electric field in metallic nanoparticles. *Ann. Phys.* **2013**, *525*, 151-161.

(129) Lin, J.; Weber, N.; Wirth, A.; Chew, S. H.; Escher, M.; Merkel, M.; Kling, M. F.; Stockman, M. I.; Krausz, F.; Kleineberg, U.: Time of flight-photoemission electron microscope for ultrahigh spatiotemporal probing of nanoplasmonic optical fields. *J. Phys. Cond. Mat.* **2009**, *21*, 314005.

(130) Chew, S. H.; Süßmann, S.; Späth, C.; Wirth, A.; Schmidt, J.; Zherebtsov, S.; Guggenmos, A.; Oelsner, A.; Weber, N.; Kapaldo, J.; Gliserin, A.; Stockman, M. I.; Kling, M. F.; Kleineberg, U.: Time-of-flight-photoelectron emission microscopy on plasmonic structures using attosecond extreme ultraviolet pulses. *Appl. Phys. Lett.* **2012**, *100*, 051904.

(131) Mikkelsen, A.; Schwenke, J.; Fordell, T.; Luo, G.; Klünder, K.; Hilner, E.; Anttu, N.; Zakharov, A. A.; Lundgren, E.; Mauritsson, J.; Andersen, J. N.; Xu, H. Q.; L'Huillier, A.: Photoemission electron microscopy using extreme ultraviolet attosecond pulse trains. *Rev. Sci. Instr.* **2009**, *80*, 123703.